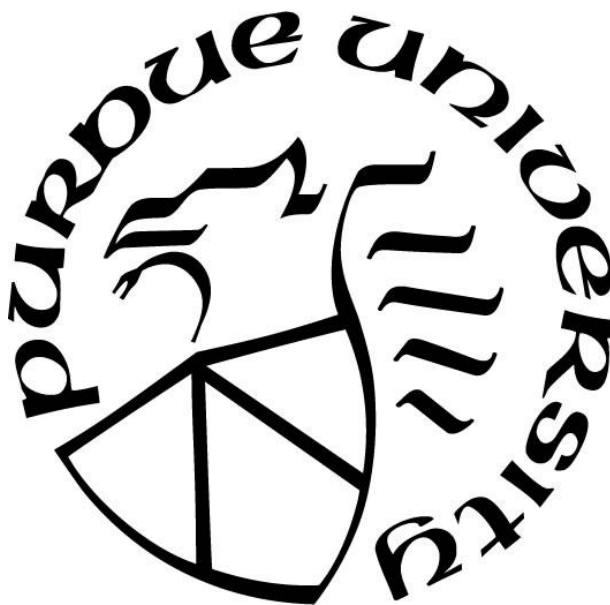# THE THERMAL SAFETY UNDERSTANDING OF MXENE ANODES IN LITHIUM-ION BATTERIES

by

Lirong Cai

A Thesis

Submitted to the Faculty of Purdue University

In Partial Fulfillment of the Requirements for the degree of

Master of Science

Davidson School of Chemical Engineering

West Lafayette, Indiana

August 2020

THE PURDUE UNIVERSITY GRADUATE SCHOOL
STATEMENT OF COMMITTEE APPROVAL

Dr. Vilas G. Pol, Chair

Davidson School of Chemical Engineering

Dr. Jeffrey T. Miller

Davidson School of Chemical Engineering

Dr. Partha P. Mukherjee

School of Mechanical Engineering

Approved by:

Dr. John A. Morgan

To my family and friends for their moral support

ACKNOWLEDGMENTS

TABLE OF CONTENTS

LIST OF TABLES

LIST OF FIGURES

ABSTRACT

Rechargeable lithium ion batteries (LIBs) are widely used in various daily life applications including electronic portable devices, cell phones, military applications, and electric vehicles throughout the world. The demand for building a safer and higher volumetric/gravimetric energy density LIBs has increased exponentially for electronic devices and electric vehicles. With the high energy density and longer cycle life, the LIBs are the most prominent energy storage system for electric vehicles. Researchers are further exploring for new materials with a high specific capacity, the MXene has been a promising new anode material for LIBs. The typical MXene material $Ti_3C_2T_z$ has 447mAh/g theoretical capacity, which is higher than traditional graphite (372 mAh/g for LiC_6) based anode.

Though LIBs are used in most of the portable energy storage devices, LIBs are still having thermal runaway safety concern, which is caused by three main reasons: mechanical, electrical, and thermal abuse. The thermal runaway is caused by the initiation of solid electrolyte interface (SEI) degradation above 80 °C on the anode surface, generating exothermic heat, and further increasing battery temperature. The SEI is a thin layer formed on anode due to electrolyte decomposition during first few charging cycles. Its degradation at low temperature generates heat inside the LIBs and triggers the thermal runaway. The thermal runaway follows SEI degradation, electrolyte reactions, polypropylene separator melting, cathode decomposition and finally leads to combustion. The thermal runaway mechanism of graphite, which is the most common and commercialized anode material of LIBs, has been studied for years. However, the thermal safety aspects of the new MXene material has not been investigated yet.

In this thesis, we primarily used differential scanning calorimetry (DSC) and specially designed multi module calorimetry (MMC) to measure exothermic and endothermic heat generated at $Ti_3C_2T_z$ anode, associated with multiple chemical reactions as the temperature increases. The *in-situ* MMC technique is employed to study the interactions and chemical reactions of all the components (separator, electrolyte, cathode and MXene anode) in the coin cell for the first time, while the *ex-situ* DSC is used to investigate the reactions happened on anode side, including electrolyte, PVDF binder, MXene, SEI and intercalated Li. Along with other complementary instruments and methods, the morphological, structural and compositional studies are carried out using X-ray diffraction (XRD), Raman spectroscopy, scanning electron microscope

(SEM), energy-dispersive X-ray spectroscopy (EDX), Brunauer-Emmett-Teller (BET) surface area measurement and electrochemical measurement to support the thermal analysis. The electrochemical and thermal runaway mechanism of conventional graphitic anode is studied and used for comparison with MXene anodes.

The $Ti_3C_2T_z$ thermal runaway is triggered by SEI decomposition around 120 °C analogous to conventional graphite. The thermal behavior of $Ti_3C_2T_z$ anode is highly dependent on electrode material, surface area, lithiation states, surface morphology, structure and surface-terminating functional groups on $Ti_3C_2T_z$, which provides more active lithium sites for exothermic reactions with the electrolyte. Especially the terminal groups (-OH, -F, =O, etc.) from the etching process affect the lithium ion intercalation and thermal runaway mechanism. With annealing treatment, the surface-terminating functional groups are modified and can achieve less exothermic heat release. By normalizing the total heat generation by specific capacities of the anode materials, it is observed that $Ti_3C_2T_z$ (2.68 J/mAh) generates slightly less exothermic heat than graphite (2.72 J/mAh) indicating slightly safer nature of $Ti_3C_2T_z$ anode. The *in-situ* thermal analysis results on the $Ti_3C_2T_z$ half-cell exhibited less total heat generation per mass (1.56 kJ/g) compared to graphite (1.59 kJ/g) half-cell.

CHAPTER 1. INTRODUCTION TO ENERGY STORAGE SYSTEM AND LIB

1.1 Energy storage system and LIB

As the demand for portable device has been increasing, the requirement of energy storage techniques is emerging. For different usage, the battery in energy storage system has been divided into primary batteries and secondary batteries. The primary battery is referring to the battery is not rechargeable. In contrast, secondary batteries are rechargeable batteries. Additionally, because of the increasing demand for pure battery vehicles (BEVs) and hybrid battery vehicles (HEVs), the demand for lithium ion battery has increased rapidly. The huge demand increasing the research on high energy density secondary batteries.

There are different types of secondary batteries, including lead acid, nickel-cadmium and alkali metal batteries. Lead acid battery as the first type of rechargeable battery has the advantage of its low price, robustness and environmental benign, so lead acid battery usually applied on golf cars and uninterruptible power supplies (UPS). However, the low specific energy limited its application to electric vehicles. Here, we introduce another type of secondary batteries: Lithium ion battery (LIB). Among all the different secondary batteries, Lithium ion battery (LIB) is the most promising one for electric vehicle application due to its high energy density, no memory effect and high cycling stability.

In 1991, the first commercial type lithium ion battery was introduced by Sony in Japan. Since then, the lithium ion battery has been applied in many different fields, especially portable devices such as cell phones and laptops. The new emerging requirement for electric vehicles also increased demand and research of lithium ion battery. Researches are seeking higher energy density materials to satisfy the requirement of longer drive distance per charge.

Even though lithium ion battery has numerous advantages, lithium ion battery still has its own concern on the safety issue. The catastrophic accidents happened in the past few years, including Tesla self-ignited, the Boeing 787 electric fire and Samsung smart phone explosion hindered the acceptance of LIBs in the market. Therefore, it is important to study battery safety. High energy density materials in lithium ion battery provide lighter weight, but at the same time

have lower thermal stability and tendency to lead thermal runaway[1]. The thermal runaway is usually triggered by abusive use including: 1) mechanical abuse, 2) electric abuse and 3) thermal abuse[1]. The mechanical abuse usually involves the deformation of battery and triggers internal short circuit. The internal short circuit as a feature of electric abuse will release the heat and increase battery inner temperature. The thermal abuse condition related to temperature increase and then lead to thermal runaway in the end[1].

1.2 Thermal safety in lithium ion battery

The overheating of battery usually increases the internal temperature of battery and leads to the thermal runaway. At the beginning, a thin passivation layer on anode surface called solid electrolyte interphase (SEI) decomposes and releases more heat triggering the entire thermal runaway[2][3]. The decomposition of SEI produces heat and increases the battery temperature. At the elevated temperature, the electrolyte will react with intercalated Li and further increase the temperature[3]. Graphite as a typical anode material for LIBSs, the thermal runaway of graphite has been investigated thoroughly in LIBs system. The SEI decomposition of graphite in $LiPF_6$ EC/DEC electrolyte system is proposed as the following reactions[4][5], which generally happened around 100 °C.

$$(CH_2OCO_2Li)_2 \rightarrow Li_2CO_3 + C_2H_4 + CO_2 + 0.5\ O_2 \tag{1.1}$$

$$2Li + (CH_2OCO_2Li)_2 \rightarrow\ 2Li_2CO_3 +\ C_2H_4 \tag{1.2}$$

$$Li_2CO_3 + PF_5 \rightarrow 2LiF + POF_3 + CO_2 \tag{1.3}$$

$$(CH_2OCO_2Li)_2 + PF_5 \rightarrow 2LiF + C_2H_4F_2 + 2POF_3 + 2CO_2 \tag{1.4}$$

$$ROCO_2Li + PF_5 \rightarrow\ LiF + RF + POF_3 +\ CO_2\ (R = CH_3\ or\ C_2H_5) \tag{1.5}$$
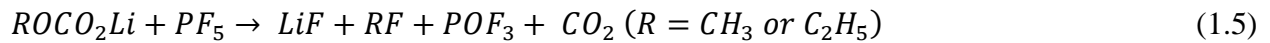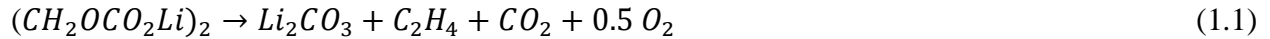
The following reaction between intercalated Li and electrolyte (EC) at higher temperature (over 200 °C) [6][7][8]:

$$2Li\ +\ C_3H_4O_3 \rightarrow\ Li_2CO_3\ + C_2H_4 \tag{2.6}$$

1.3 Dissertation overview

This thesis is motivated by the increasing concern related to lithium ion battery safety, especially on the thermal safety. The understanding the anode thermal runaway is essential for thermal safety research. As new anode material keeps emerging over the year, the thermal safety of those material has not been investigated yet. It's important to elucidate the thermal runaway process of the new anode material: MXene. Chapter 2 will provide a literature background of the MXene material including the synthesis process and its properties. Also, the MXene's applications and characteristics in lithium ion battery applications, involving the electrochemical and thermal behaviors. Chapter 3 presents my work in elucidating the unknown thermal runaway process of $Ti_3C_2T_z$ MXene in lithium ion battery. The exothermic and endothermic reactions have been investigated using differential scanning calorimetry (DSC) and multiple module calorimetry (MMC) to present a detailed and integrated picture. Also, we presented a method to improve the safety and electrochemical performance of $Ti_3C_2T_z$ and demonstrated it is better than graphite. Chapter 4 summarized the thesis and provided insightful thoughts about possible future research.

1.4 Reference

[1]   X. Feng, M. Ouyang, X. Liu, L. Lu, Y. Xia, X. He, Thermal runaway mechanism of lithium ion battery for electric vehicles: A review, Energy Storage Mater. 10 (2018) 246–267. https://doi.org/10.1016/j.ensm.2017.05.013.

[2]   K. Liu, Y. Liu, D. Lin, A. Pei, Y. Cui, Materials for lithium-ion battery safety, Sci. Adv. 4 (2018). https://doi.org/10.1126/sciadv.aas9820.

[3]   R.A. Adams, A. Varma, V.G. Pol, Carbon Anodes for Nonaqueous Alkali Metal-Ion Batteries and Their Thermal Safety Aspects, Adv. Energy Mater. 1900550 (2019) 1900550. https://doi.org/10.1002/aenm.201900550.

[4]   M.N. Richard, J.R. Dahn, Accelerating rate calorimetry study on the thermal stability of lithium intercalated graphite in electrolyte. I. Experimental, J. Electrochem. Soc. 146 (1999) 2068–2077. https://doi.org/10.1149/1.1391893.

[5]   C. Forestier, S. Grugeon, C. Davoisne, A. Lecocq, G. Marlair, M. Armand, L. Sannier, S. Laruelle, Graphite electrode thermal behavior and solid electrolyte interphase investigations: Role of state-of-the-art binders, carbonate additives and lithium bis(fluorosulfonyl)imide salt, J. Power Sources. 330 (2016) 186–194. https://doi.org/10.1016/j.jpowsour.2016.09.005.

[6]   R.A. Adams, A. Varma, V.G. Pol, Mechanistic elucidation of thermal runaway in potassium-ion batteries, J. Power Sources. 375 (2018) 131–137. https://doi.org/10.1016/j.jpowsour.2017.11.065.

[7]   H.H. Lee, C.C. Wan, Y.Y. Wang, Thermal Stability of the Solid Electrolyte Interface on Carbon Electrodes of Lithium Batteries, J. Electrochem. Soc. 151 (2004) 542–547. https://doi.org/10.1149/1.1647568.

[8]   H. Wang, D. Yu, C. Kuang, L. Cheng, W. Li, X. Feng, Z. Zhang, X. Zhang, Y. Zhang, Alkali Metal Anodes for Rechargeable Batteries, Chem. 5 (2019) 313–338. https://doi.org/10.1016/j.chempr.2018.11.005.

CHAPTER 2. MXENE ANODE AND SAFETY

2.1 Novel 2D material MXene

With the rapid development of portable devices and electric vehicles, the demand on higher specific capacity material for lithium ion battery is growing. MXene is one of the new 2D material, which can be used as LIB anode. MXene discovered by Yury Gogotsi at Drexel University in 2011 are produced from MAX phase material by selectively etching out the A atoms[1][2][3]. The $M_{n+1}AX_n$ is the typical formula of MAX phase, where M stands for transition metal, A represents the A-group element, and X is carbon or nitrogen, as n equals to 1, 2, or 3. The interlayer M-A bonds and interatomic A-A bonds are weaker than the strong covalent/metallic/ionic M-X bond, resulting more chemically reactive of A layer and providing the opportunity of etching[4]. The MAX phase materials are layered carbides or nitrides, so the MXenes can remain the layer structure after etching process. Typically, the hydrofluoric acid (HF) and etching is the common approach of etching. After HF etching, the A-group atoms were exfoliated from the structure, resulting in MXenes in the form of $M_{n+1}X_nT_x$. The T represents the surface terminal groups, such as OH, F, and O. In 2011, the first MXene $Ti_3C_2T_z$ was reported by Yury Gogotsi and his co-worker by using HF etching on Ti_3AlC_2 [1]. The HF etching method has the $Ti_3C_2T_z$ with surface terminal groups of OH, O and F [2]. With different HF concentrations (from 5 wt. % to 30 wt. %), the etching time varies from 24 hours to 5 hours[5]. The higher concentration of HF can compress the etching time, but also results in different thermal properties [6]. The novel synthesis method *in-situ* HF etching can avoid direct HF use and have the clay form of $Ti_3C_2T_x$ [5]. Another synthesis method for MXenes from MAX phase is high temperature etching. The Ti_4N_3 can be synthesized from Ti_4AlN_3 in a fluoride salt at 550 °C [7].

Because etching methods contain acidic-fluoride solution, the MXenes have the surface terminal groups of -OH, -O and -F, presented by T_z in the formula. $Ti_3C_2T_z$ as the first and most common MXene, the surface terminal groups has been studied that they are randomly distributed rather than gathered in specific region by groups or atoms [8]. The quantity of terminal groups is highly depends on the synthesis method and the amount of -OH group with hydrogen bonded water is less than -O and -F, which is directly bonded on the surface [9][10]. With NMR study, the HF etching $Ti_3C_2T_z$ has four times of -F group than LiF-HCl etching [10]. The surface terminal groups'

thermal stability was analyzed by thermal gravimetric analysis (TGA) in $Ti_3C_2T_z$ case. In 30% HF etching condition, the onset temperature of water release is at 100 °C, decreasing from 200 °C for 10% HF etching and 320 °C for 5% HF etching [6]. The accordion-like multilayer $Ti_3C_2T_z$ morphology has more site for multilayer water storage[6].

The surface terminal groups together with nature of M, X element decides the electric properties, because the high conductivity is achieved by good contact of individual and large flake size [11]. The first principle calculation demonstrates the thicker layer MXene with higher number of transition metal, such as Ti_3C_2, Ti_4C_3, Ti_4N_3, V_3C_2, has high electronic conductivity and can promote ionic and electronic conductivities [12]. For example, the mild etching method $Ti_3C_2T_z$ can have 4600 S/cm [13], but the individual $Ti_3C_2T_z$ flake with few defects reveals high conductivity up to 6500 S/cm [14].

2.2 MXene's applications

With these unique properties of MXenes, they can be applied on many different field, including energy storage system[15], photothermal conversion[16], water purification[17] and electromagnetic interference (EMI)[13]. Particularly, the self-floating $Ti_3C_2T_z$ thin membrane shows the 100% light-to-heat conversion and 84% light-to-water evaporation efficiency [16]. The anodic aluminum oxide (AAO) supported MXene membrane exhibit more than 1000 Lm^{-2} h^{-1} bar^{-1} water permeance, over 90% rejection rate for >2.5 nm molecule size and stable long-time operation for water purification[17]. The $Ti_3C_2T_z$ can use as EMI shielding in 45 micrometer think film and demonstrate 92 decibels effectiveness due to its high electrical conductivity and internal reflections in free-standing film[13]. Because MXenes exhibit good mechanical flexibility, they can be applied on different shape of surface with high effectiveness[13].

The MXene materials with good electrical conductivity, hydrophilic nature and high mechanical strength[18] has been experimentally and theoretically proved to be good candidate of next-generation-promising materials for energy storage system including supercapacitors [19], LIBs [4] sodium-ion batteries (SIBs) [20]and potassium-ion batteries (PIBs) [21]. As MXenes have their unique properties including metallic conductivities, hydrophilic surface and large surface area [22], MXenes also has the potential in supercapacitor application. The layered structure of MXene has the capability to intercalate lithium ions, serving similar functions as

graphite. Especially the large interlayer spacing not only provides the accessible site and route for alkali ion transportation and intercalation, but also can have small organic atoms intercalation. This feature also opens the door for alkali ions with larger size, such as SIBs and PIBs with high theoretical capacity. For example, the $Ti_3C_2T_z$ can achieve 351.8 mAh/g theoretical capacity in SIB and 191.8 mAh/g theoretical capacity in PIB [23]. Both theoretical capacities are higher than the traditional material graphite (35 mAh/g in SIB for NaC_{64} and 279 mAh/g in PIBs for KC_8)[24][25].

Electrode as a major component in battery system, there are tremendous researches on discovering novel materials for higher lithium storage ability and better ion conductivity[4]. Among the rechargeable batteries' applications, lithium ion batteries are the most popular application for 2D MXene. The publication number on 2D MXene and its composite in lithium ion batteries is over 300 [4]. MXenes also have intrinsic advantages of 2D materials including the acceible charge carries interaction, high surface area and rapid ion transportation. These properties combined with the larger interlayer spacing (1.25 nm of $Ti_3C_2T_z$ [21]) compared to other 2D material (graphene 0.335 nm [24]) provide the opportunities for fast ion transportation and fast-charge batteries. The DFT calculation demonstrates the Li storage in Ti_3C_2 by Li intercalating into the space vacated by Al layer and results in the formation of $Ti_3C_2Li_2$ with 320 mAh/g theoretical capacity by equation (2.1) [1].

$$Ti_3C_2 + 2Li \rightarrow Ti_3C_2Li_2 \tag{2.1}$$

Because large effective ion radius lowers the maximum adatom content and increases interaction between lithium atoms, with the consideration of effective ion radius and maximum adatom content of Li, Ti_3C_2 can represent higher theoretical capacity of 447.8 mAh/g [23]. The DFT study also reveals the effect of surface-terminating groups on Li storage in Ti_3C_2. The bare monolayer Ti_3C_2 without surface-terminating groups is the best candidate for LIBs because of its high theoretical Li capacity with electrical conductivity, low diffusion barrier and low open circuit voltage [26]. The -OH and -F surface-terminating groups have a tendency to degrade the Li diffusion, therefore decreasing the capacity [26]. $Ti_3C_2T_z$ with O surface-terminating exhibit the highest capacity because extra Li absorbed by lithiated O form an additional layer corresponding to high Li storage capacity especially in delaminate case, which has large accessible surface [27].

In order to achieve higher capacity, MXenes usually combined with other anode materials, such as the transition metal oxides (TMOs). For example, SnO_2 and $Ti_3C_2T_z$ are combined together as the anode for capacity 1030 mAh/g at 100 mA/g for the first cycle[28]. Because SnO_2 is nontoxic, economic and environmental benign, SnO_2 is a good candidate to combine with $Ti_3C_2T_z$ [28]. Typically, lithium ions are able to intercalate and deintercalate into MXenes layer phases with high surface diffusion rate, resulting in comparably high capacity in experiment [15] [29]. Table. 2.1 presents the specific capacities of several different MXene electrodes in LIBs using 1M $LiPF_6$ electrolyte. Both Ti_3C_2 and Nb_2C showed higher capacity than graphite, which has a theoretical capacity of 372 mAh/g for LiC_6 [30].

Table 2.1 Specific capacity of different MXenes electrode

Electrode Material	Specific capacity (mAh/g)	Ref
$Ti_3C_2T_x$	410 at 1C	[31]
Nb_2C/CNT	420 at 0.5C	[32]
V_2C	254 at 0.2C	[33]
Ti_2C	65 at 10C	[29]

2.3 MXene's thermal behavior

For safety aspects, the thermal stability and terminal groups' behavior of MXene at high temperature are essential $Ti_3C_2T_z$ and thermal runaway in LIBs. The thermal gravimetric (TG) analysis, mass spectrometry (MS) analysis and differential scanning calorimetric (DSC) is primarily used to reveal the thermal stability coupled with other complimentary method SEM and XRD. The thermal stability and surface chemistry of $Ti_3C_2T_z$ has been studied under high temperature via TG-MS analysis[6][34][35][36]. For 5 wt% etched $Ti_3C_2T_z$, the weight loss started at 320 °C corresponding to release of structural water [6]. The second weight loss happened at 530 °C, which is the onset temperature of surface group (-OH) dissociation, including O_2 and H_2 gas release[6]. At 750 °C, with CO_2 release, $Ti_3C_2T_z$ structure started degrading and finally converted to TiC cubic structure at 1100 °C. With increasing concentration (5% to 30%) of HF acid in etching process, the structural water release decreases from 320 °C to 100 °C and other

18

terminal groups decomposition temperature decreases [6]. At 30 wt% HF etching, there is larger amount of water released and F terminal group release around 500 °C. Also, HF concentration affects the surface terminal groups bonding and percentage, such as increasing in strongly bonded water molecules, but the terminal group could be modified by heat treatment and achieve higher capacity[37]. Even though there is a few investigations on the thermal behavior of $Ti_3C_2T_z$, the thermal runaway mechanism on Ti_3C_2 has not been studied yet in LIBs. This feature is important for the $Ti_3C_2T_z$ anode safety when we consider it as the next-generation material for energy storage system.

2.4 References

[1]   M. Naguib, M. Kurtoglu, V. Presser, J. Lu, J. Niu, M. Heon, L. Hultman, Y. Gogotsi, M.W. Barsoum, Two-dimensional nanocrystals produced by exfoliation of Ti 3AlC 2, Adv. Mater. 23 (2011) 4248–4253. https://doi.org/10.1002/adma.201102306.

[2]   M. Naguib, O. Mashtalir, J. Carle, V. Presser, J. Lu, L. Hultman, Y. Gogotsi, M.W. Barsoum, Two-dimensional transition metal carbides, ACS Nano. 6 (2012) 1322–1331. https://doi.org/10.1021/nn204153h.

[3]   M. Naguib, J. Halim, J. Lu, K.M. Cook, L. Hultman, Y. Gogotsi, M.W. Barsoum, New two-dimensional niobium and vanadium carbides as promising materials for li-ion batteries, J. Am. Chem. Soc. 135 (2013) 15966–15969. https://doi.org/10.1021/ja405735d.

[4]   D. Xiong, X. Li, Z. Bai, S. Lu, Recent Advances in Layered Ti3C2Tx MXene for Electrochemical Energy Storage, Small. 14 (2018) 1–29. https://doi.org/10.1002/smll.201703419.

[5]   M. Alhabeb, K. Maleski, B. Anasori, P. Lelyukh, L. Clark, S. Sin, Y. Gogotsi, Guidelines for Synthesis and Processing of Two-Dimensional Titanium Carbide (Ti 3 C 2 T x MXene), Chem. Mater. 29 (2017) 7633–7644. https://doi.org/10.1021/acs.chemmater.7b02847.

[6]   M. Seredych, C.E. Shuck, D. Pinto, M. Alhabeb, E. Precetti, G. Deysher, B. Anasori, N. Kurra, Y. Gogotsi, High-Temperature Behavior and Surface Chemistry of Carbide MXenes Studied by Thermal Analysis, Chem. Mater. 31 (2019) 3324–3332. https://doi.org/10.1021/acs.chemmater.9b00397.

[7]   P. Urbankowski, B. Anasori, T. Makaryan, D. Er, S. Kota, P.L. Walsh, M. Zhao, V.B. Shenoy, M.W. Barsoum, Y. Gogotsi, Synthesis of two-dimensional titanium nitride Ti4N3 (MXene), Nanoscale. 8 (2016) 11385–11391. https://doi.org/10.1039/c6nr02253g.

[8]   H.W. Wang, M. Naguib, K. Page, D.J. Wesolowski, Y. Gogotsi, Resolving the Structure of Ti3C2Tx MXenes through Multilevel Structural Modeling of the Atomic Pair Distribution Function, Chem. Mater. 28 (2016) 349–359. https://doi.org/10.1021/acs.chemmater.5b04250.

[9]   B. Anasori, M.R. Lukatskaya, Y. Gogotsi, 2D metal carbides and nitrides (MXenes) for energy storage, Nat. Rev. Mater. 2 (2017). https://doi.org/10.1038/natrevmats.2016.98.

[10]   M.A. Hope, A.C. Forse, K.J. Griffith, M.R. Lukatskaya, M. Ghidiu, Y. Gogotsi, C.P. Grey, NMR reveals the surface functionalisation of Ti3C2 MXene, Phys. Chem. Chem. Phys. 18 (2016) 5099–5102. https://doi.org/10.1039/c6cp00330c.

[11]   X. Sang, Y. Xie, M.W. Lin, M. Alhabeb, K.L. Van Aken, Y. Gogotsi, P.R.C. Kent, K. Xiao, R.R. Unocic, Atomic defects in monolayer titanium carbide (Ti3C2Tx) MXene, ACS Nano. 10 (2016) 9193–9200. https://doi.org/10.1021/acsnano.6b05240.

[12]   J. Nan, X. Guo, J. Xiao, X. Li, W. Chen, W. Wu, H. Liu, Y. Wang, M. Wu, G. Wang, Nanoengineering of 2D MXene-Based Materials for Energy Storage Applications, Small. 1902085 (2019) 1–20. https://doi.org/10.1002/smll.201902085.

[13]   F. Shahzad, M. Alhabeb, C.B. Hatter, B. Anasori, S.M. Hong, C.M. Koo, Y. Gogotsi, Electromagnetic interference shielding with 2D transition metal carbides (MXenes), Science (80-.). 353 (2016) 1137–1140. https://doi.org/10.1126/science.aag2421.

[14]   A.D. Dillon, M.J. Ghidiu, A.L. Krick, J. Griggs, S.J. May, Y. Gogotsi, M.W. Barsoum, A.T. Fafarman, Highly Conductive Optical Quality Solution-Processed Films of 2D Titanium Carbide, Adv. Funct. Mater. 26 (2016) 4162–4168. https://doi.org/10.1002/adfm.201600357.

[15]   M. Naguib, B. Dyatkin, V. Presser, M.W. Barsoum, P. Simon, Y. Gogotsi, J. Come, P.-L. Taberna, MXene: a promising transition metal carbide anode for lithium-ion batteries, Electrochem. Commun. 16 (2012) 61–64. https://doi.org/10.1016/j.elecom.2012.01.002.

[16]   R. Li, L. Zhang, L. Shi, P. Wang, MXene Ti3C2: An Effective 2D Light-to-Heat Conversion Material, ACS Nano. 11 (2017) 3752–3759. https://doi.org/10.1021/acsnano.6b08415.

[17]   L. Ding, Y. Wei, Y. Wang, H. Chen, J. Caro, H. Wang, A Two-Dimensional Lamellar Membrane: MXene Nanosheet Stacks, Angew. Chemie. 129 (2017) 1851–1855. https://doi.org/10.1002/ange.201609306.

[18]   X. Wang, T.S. Mathis, K. Li, Z. Lin, L. Vlcek, T. Torita, N.C. Osti, C. Hatter, P. Urbankowski, A. Sarycheva, M. Tyagi, E. Mamontov, P. Simon, Y. Gogotsi, Influences from solvents on charge storage in titanium carbide MXenes, Nat. Energy. 4 (2019) 241–248. https://doi.org/10.1038/s41560-019-0339-9.

[19]   J. Xu, N. Yang, S. Heuser, S. Yu, A. Schulte, H. Schönherr, X. Jiang, Achieving Ultrahigh Energy Densities of Supercapacitors with Porous Titanium Carbide/Boron-Doped Diamond Composite Electrodes, Adv. Energy Mater. 9 (2019) 1–11. https://doi.org/10.1002/aenm.201803623.

[20]   S. Kajiyama, L. Szabova, K. Sodeyama, H. Iinuma, R. Morita, K. Gotoh, Y. Tateyama, M. Okubo, A. Yamada, Sodium-Ion Intercalation Mechanism in MXene Nanosheets, ACS Nano. 10 (2016) 3334–3341. https://doi.org/10.1021/acsnano.5b06958.

[21] P. Lian, Y. Dong, Z.S. Wu, S. Zheng, S. Wang, C. Sun, J. Qin, X. Shi, X. Bao, Alkalized Ti3C2 MXene nanoribbons with expanded interlayer spacing for high-capacity sodium and potassium ion batteries, Nano Energy. 40 (2017) 1–8. https://doi.org/10.1016/j.nanoen.2017.08.002.

[22] D. Xiong, X. Li, Z. Bai, S. Lu, Recent Advances in Layered Ti3C2Tx MXene for Electrochemical Energy Storage, Small. 14 (2018) 1–29. https://doi.org/10.1002/smll.201703419.

[23] D. Er, J. Li, M. Naguib, Y. Gogotsi, V.B. Shenoy, Ti3C2 MXene as a high capacity electrode material for metal (Li, Na, K, Ca) ion batteries, ACS Appl. Mater. Interfaces. 6 (2014) 11173–11179. https://doi.org/10.1021/am501144q.

[24] R.A. Adams, A. Varma, V.G. Pol, Carbon Anodes for Nonaqueous Alkali Metal-Ion Batteries and Their Thermal Safety Aspects, Adv. Energy Mater. 1900550 (2019) 1900550. https://doi.org/10.1002/aenm.201900550.

[25] Z. Jian, W. Luo, X. Ji, Carbon Electrodes for K-Ion Batteries, J. Am. Chem. Soc. 137 (2015) 11566–11569. https://doi.org/10.1021/jacs.5b06809.

[26] Q. Tang, Z. Zhou, P. Shen, Are MXenes promising anode materials for Li ion batteries? Computational studies on electronic properties and Li storage capability of Ti 3C 2 and Ti 3C 2X 2 (X = F, OH) monolayer, J. Am. Chem. Soc. 134 (2012) 16909–16916. https://doi.org/10.1021/ja308463r.

[27] Y. Xie, M. Naguib, V.N. Mochalin, M.W. Barsoum, Y. Gogotsi, X. Yu, K.W. Nam, X.Q. Yang, A.I. Kolesnikov, P.R.C. Kent, Role of surface structure on li-ion energy storage capacity of two-dimensional transition-metal carbides, J. Am. Chem. Soc. 136 (2014) 6385–6394. https://doi.org/10.1021/ja501520b.

[28] F. Wang, Z. Wang, J. Zhu, H. Yang, X. Chen, L. Wang, C. Yang, Facile synthesis SnO2 nanoparticle-modified Ti3C2 MXene nanocomposites for enhanced lithium storage application, J. Mater. Sci. 52 (2017) 3556–3565. https://doi.org/10.1007/s10853-016-0369-7.

[29] J. Come, M. Naguib, P. Rozier, M.W. Barsoum, Y. Gogotsi, P.-L. Taberna, M. Morcrette, P. Simon, A Non-Aqueous Asymmetric Cell with a Ti 2 C-Based Two-Dimensional Negative Electrode , J. Electrochem. Soc. 159 (2012) A1368–A1373. https://doi.org/10.1149/2.003208jes.

[30] R.A. Adams, A. Varma, V.G. Pol, Mechanistic elucidation of thermal runaway in potassium-ion batteries, J. Power Sources. 375 (2018) 131–137. https://doi.org/10.1016/j.jpowsour.2017.11.065.

[31] O. Mashtalir, M. Naguib, V.N. Mochalin, Y. Dall'Agnese, M. Heon, M.W. Barsoum, Y. Gogotsi, Intercalation and delamination of layered carbides and carbonitrides, Nat. Commun. 4 (2013) 1–7. https://doi.org/10.1038/ncomms2664.

[32] M.R. Lukatskaya, Y. Gogotsi, M.W. Barsoum, O. Mashtalir, M.-Q. Zhao, Amine-Assisted Delamination of Nb 2 C MXene for Li-Ion Energy Storage Devices , Adv. Mater. 27 (2015) 3501–3506. https://doi.org/10.1002/adma.201500604.

[33] J. Zhou, S. Gao, Z. Guo, Z. Sun, Ti-enhanced exfoliation of V2AlC into V2C MXene for lithium-ion battery anodes, Ceram. Int. 43 (2017) 11450–11454. https://doi.org/10.1016/j.ceramint.2017.06.016.

[34] K. Wang, Y. Zhou, W. Xu, D. Huang, Z. Wang, M. Hong, Fabrication and thermal stability of two-dimensional carbide Ti3C2 nanosheets, Ceram. Int. 42 (2016) 8419–8424. https://doi.org/10.1016/j.ceramint.2016.02.059.

[35] J. Li, Y. Du, C. Huo, S. Wang, C. Cui, Thermal stability of two-dimensional Ti2C nanosheets, Ceram. Int. 41 (2015) 2631–2635. https://doi.org/10.1016/j.ceramint.2014.10.070.

[36] Z. Li, L. Wang, D. Sun, Y. Zhang, B. Liu, Q. Hu, A. Zhou, Synthesis and thermal stability of two-dimensional carbide MXene Ti3C2, Mater. Sci. Eng. B Solid-State Mater. Adv. Technol. 191 (2015) 33–40. https://doi.org/10.1016/j.mseb.2014.10.009.

[37] F. Kong, X. He, Q. Liu, X. Qi, Y. Zheng, R. Wang, Y. Bai, Improving the electrochemical properties of MXene Ti 3 C 2 multilayer for Li-ion batteries by vacuum calcination, Electrochim. Acta. 265 (2018) 140–150. https://doi.org/10.1016/j.electacta.2018.01.196.

CHAPTER 3. MECHANISTIC ELUCIDATION OF THERMAL SAFETY OF TI3C2TZ MXENE ANODES IN LITHIUM-ION BATTERIES

Material synthesis was carried out by Kaitlyn Prenger. Material characterization, electrochemical testing, data analysis was carried out by Lirong Cai. Lirong Cai, Zheng Li, Sensen Zhang and Kailyn Prenger contributed to the preparation and revision of manuscript.

3.1 Summary

$Ti_3C_2T_z$, as a new emerging two-dimensional MXene, is a promising lithium-ion battery (LIB) anode material with excellent electrochemical performance. For the first time, the thermal behavior of $Ti_3C_2T_z$ anode in LIBs is systematically studied using specially designed *in-situ* multiple module calorimetry (MMC) and *ex-situ* differential scanning calorimetry (DSC). The $Ti_3C_2T_z$ thermal runaway is triggered by the solid electrolyte interphase (SEI) decomposition due to increase in the cell temperature following a series of chemical reactions. The thermal behavior of $Ti_3C_2T_z$ anode is highly dependent on electrode material, its surface area, lithiation states, surface morphology, structure and surface-terminating functional groups on $Ti_3C_2T_z$, which provides more active lithium sites for exothermic reactions with the electrolyte. After the annealing process, the $Ti_3C_2T_z$ anode with modified surface-terminating functional groups is slightly safer than the graphitic anode. The *in-situ* thermal analysis results on the $Ti_3C_2T_z$ half-cell exhibited less total heat generation per mass (1.56 kJ g^{-1}) compared to graphite (1.59 kJ g^{-1}) half-cell.

3.2 Introduction

The 2019 Chemistry Nobel Prize-winning rechargeable lithium-ion battery (LIB) technology is widely used in portable electronic devices, electric vehicles, and grid energy storage applications [1–4]. Significant advantages of conventional graphite anode like facile synthesis, commercially inexpensive sources, and environmentally benign properties give it great success in the market. However, increasing demand from the energy storage market requires advanced LIBs with higher energy density, cycling stability, and rate capability, leading to the intensive exploration of next-generation anode materials. Two dimensional carbides and nitrides, known as MXenes, feature

unique two-dimensional (2D) morphology, hydrophilic features, high electronic conductivity, and favorable mechanical strength have been reported to be promising anode materials for LIBs [5].

MXenes are a newly emerged family of 2D materials composed of transition metal carbides or nitrides. Similar to graphite, their suitable interlayer space allows the intercalation of alkali metal ions, thus endowing them great potential as anode materials for secondary alkali ion batteries [6–8]. Their electrochemical performance has been successfully demonstrated in various types of energy storage devices like LIBs [9], supercapacitors [10,11] sodium-ion batteries (SIBs) [12,13], and potassium ion batteries (KIBs) [14,15]. Among all the MXene materials, $Ti_3C_2T_z$ has exhibited great promise as a LIB anode with 448 mAh g^{-1} theoretical capacity [16]. Various studies have been conducted on its properties, including the well-known etching conditions and outstanding electrochemical performance. Its high electronic conductivity (10,000 S cm^{-1}) [17], excellent Li^+ diffusion mobility ($\sim 10^{-10}$–10^{-9} cm^2 s^{-1}) [18], and low Li^+ diffusion barrier (0.07 eV) facilitate the lithiation/delitiation process.

MXenes are synthesized from their parent MAX phase ceramics using selective etching with hydrofluoric acid (HF) or similar methods to remove A layers from the MAX phase [6,19]. The typical formula of MAX phases is $M_{n+1}AX_n$, where M stands for an early transition metal, A represents the A-group element, X is carbon and/or nitrogen, and n equals 1, 2, or 3. After etching out the A-group atoms with HF, the product is a layered material in the form of $M_{n+1}X_nT_z$ is known as MXenes. Due to the etching process, surface-terminating functional groups (represented by T_z) such as OH, F, and O remained on the layered surface. Enhanced layer space in $Ti_3C_2T_z$ (15.04 Å) in contrast to graphite (3.35 Å) allows high Li^+ ion surface diffusion, resulting in high capacity and rate capability [7,19,20]. From the literature, the MXene family type materials have higher capacity compared to graphite, such as delaminated $Ti_3C_2T_z$ (410 mAh g^{-1} at 1 C) [21], multi-layer Mo_2CT_z/CNT (560 mAh g^{-1}at 1.5 C) [22], multi-layer V_2CT_z (254 mAh g^{-1}at 0.2 C) [23], and multi-layer Ti_2CT_z (65 mAh g^{-1} at 10 C) [7].

Despite the intensive studies on the electrochemical performance of MXene material, little is known regarding their thermal safety aspects, which is the most significant parameter for the commercial application. As catastrophic accidents continuously emerges, accompanied by the fast-growing LIBs market, the thermal safety has drawn great attention from society [2]. Because of anodes exothermic reactions are known to be initiating reactions of the whole battery thermal runaway process, understanding the thermal behavior of MXene materials in LIB anodes is equally

important as investigating their electrochemical performance. Conventional LIBs with non-aqueous liquid electrolyte are known to be intrinsically unsafe due to the electrolyte flammability and instability under oxidative and reductive conditions. Existing thermal safety studies of conventional LIBs preliminarily revealed the thermal runaway mechanism, which is commonly initiated by three conditions: mechanical, electrical and thermal abuse [2]. At the beginning of the whole process, the exothermic reactions lose control and heat up the batteries [24]. The solid electrolyte interface (SEI) decomposition generates additional heat and exposes fresh intercalated lithium to the electrolyte [25]. Several exothermic reactions occur between lithium and electrolyte as well as polymer binders. As a result of polypropylene separator melting, internal short circuit further heats up the battery. Finally, cathode thermal decomposition leads to the combustion of electrolyte, battery fire, and explosion [24].

In this work, thermal stability and safety aspects of MXene anodes were explored through the thermal runaway mechanism study of a representative $Ti_3C_2T_z$ MXene via morphological, structural, and compositional characterization followed by detailed differential scanning calorimetry (DSC) and an *in-situ* thermal analysis technique, multiple mode calorimetry (MMC). Thermal behavior of $Ti_3C_2T_z$ MXene anode and its thermal response with other battery components (electrolyte, polymer binder, etc.) was *ex-situ* revealed by DSC, providing information including reaction temperature and heat generation [26,27]. The overview of the thermal stability of MXene anode is obtained by the *in-situ* thermal behavior study of half-cells.

3.3 Materials and Methods

3.3.1 Synthesis of MXene Ti3C2Tz

Powders of titanium (-325 mesh, Alfa Aesar), aluminum (-325 mesh, Alfa Aesar), and graphite (APS 7-11 micron, Alfa Aesar) with a 3:1.2:1.88 atomic ratio were mixed in a high-density polyethylene jar with 10 mm yttria-stabilized zirconia balls as mixing media using a Turbula T2F mixer for 3 h at 56 rpm. The mixed powders were heated to 1600 °C for 2 h at a heating rate of 10°C min^{-1} in a tube furnace with a continuous flow of argon. The product was allowed to cool to room temperature then ground to -325 mesh for etching.

To etch, 3 g of Ti_3AlC_2 was slowly added over the course of 10 minutes to 30 mL aqueous hydrofluoric acid (48-51%, Sigma Aldrich). The mixture was held at room temperature while

stirring for 18 h. After this period, the product was washed with copious deionized (DI) water through cycles of decanting acidic mixture, adding fresh DI water and centrifuging until a pH>6 was achieved. The wet powders were dried using vacuum-assisted filtration. The annealed $Ti_3C_2T_z$ samples were calcined under the Ar atmosphere at 400 °C for 20 minutes.

3.3.2 Materials characterization

The crystallinity and phase purity of synthesized MXene, $Ti_3C_2T_z$ material was examined by powder X-ray diffraction (XRD) using Rigaku SmartLab X-ray diffractometer in the 2θ from 5° to 65° (λ = 0.154 nm). Scanning electron microscopy (SEM) and energy-dispersive X-ray spectroscopy (EDX) were utilized to confirm the morphology and presence of elements in the synthesized MXene $Ti_3C_2T_z$ material at 15kV and 7.475 nA probe current using JEOL JCM-6000 Plus NeoScope Benchtop SEM. Thermo Scientific DXR Raman microscope measurement was used to determine the presence of the functional groups in MXene $Ti_3C_2T_z$ material and cycled electrodes with 633 nm laser. $Ti_3C_2T_z$ samples were degassed at 250 °C under vacuum for 24 h before performing surface area analysis. Brunauer–Emmett–Teller (BET) surface area was measured by Quantachrome Instruments NOVA 2200e using nitrogen adsorption/desorption isotherm measurements at 77K. The pore size distribution was measured by Barrette-Joynere-Halende analysis method.

3.3.2 Electrochemical measurement

Both $Ti_3C_2T_z$ and graphite electrodes were prepared by slurry, containing 10% polyvinylidene difluoride (PVDF) as a binder, 10% carbon black as a conductive additive and 80% active material ($Ti_3C_2T_z$ or graphite) in N-methyl-2-pyrrolidone (NMP) solvent. The slurry was mixed for 30 minutes with small ZrO_2 balls and cast on a copper foil using the automatic doctor blade method. The laminate was dried in a vacuum oven at 80 °C for 24 h and cut into 14 mm diameter disc electrodes. The $Ti_3C_2T_z$ and graphite electrodes were used to assemble CR 2032 coin type cells with Li metal as a reference electrode, polypropylene (PP) as the separator, and electrolyte of 1.0 M $LiPF_6$ salt in 1:1 (v/v) ethylene carbonate (EC) and diethyl carbonate (DEC) solvents. The half-cells were assembled in an Ar filled glovebox, monitored with < 2 ppm of oxygen and moisture. The coin cells were cycled galvanostatically by applying a constant current density of 20 mA g^{-1}

between 0.005 V to 3 V (vs Li/Li$^+$) at room temperature to create a uniform SEI layer for both electrodes.

3.3.3 Thermal Analysis

Differential Scanning Calorimetry (DSC) was performed to determine the thermal stability of MXene, Ti$_3$C$_2$T$_z$ and graphite materials using a TA Q20 instrument. For DSC study, the half-cells at different states of charges (SOCs) from 5 mV to 3V (*vs.* Li/Li$^+$) were dissembled in the Ar atmosphere and dried in vacuum for 5 minutes to remove extra solvent. The washout electrodes were washed in dimethyl carbonate (DMC) twice and vacuum dried overnight. The electrode materials were removed with a nonconducting spatula, collected in a DSC aluminum pan and sealed with a hermetic lid. Typically, ~1-2 mg sample was placed and measured using a microbalance for enhanced accuracy in sample weighing. The DSC tests were conducted at 5 ℃ min^{-1} from 50 ℃ to 500 ℃. Further, the *in situ* thermal analysis was performed by NETZSCH multimode calorimetry (MMC) 227. For this study, the cycled half-cells were placed into the MMC cell chamber after stabilized at a certain voltage (discharge/charge status) and allowed to heat at a constant rate (0.2 ℃ min^{-1}) from 40 ℃ to 300 ℃. The half-cells were comprised of all the electrochemically active and inactive parts, such as lithium, polypropylene separator, Ti$_3$C$_2$T$_z$/graphite anode, and electrolyte, to measure the realistic thermal runaway values.

3.4 Results and Discussion

3.4.1 Morphology and Structural characterization

The structure of synthesized Ti$_3$C$_2$T$_z$ MXene was characterized by X-ray diffraction and Raman spectroscopy. The Raman spectrum of Ti$_3$C$_2$T$_z$ sample (Fig. 3.1a) collected from 100 cm^{-1} to 1800 cm^{-1} reflected its molecular structure [19]. The band (*) at 230, 313, 615 and 707 cm^{-1} are signature bands of Ti$_3$C$_2$T$_z$, corresponding to Ti-C vibrations [28,29]. The strong band (♦) at 144 cm^{-1} belongs to TiO$_2$-Ti$_3$C$_2$T$_z$ nanocomposite or anatase TiO$_2$ [30]. The O terminations and TiO$_2$ structure in Ti$_3$C$_2$T$_z$ is known to enhance specific capacity [23–25,31].

The MAX phase (including Ti$_3$AlC$_2$) is known to have a hexagonal structure. Even after etching out the Al from Ti$_3$C$_2$T$_z$, it retains its hexagonal lattice structure [32] and *d*-spacing in *c* direction increases dramatically compared to Ti$_3$AlC$_2$ [33]. Compared with the Ti$_3$C$_2$T$_z$ XRD

profile in literature, all the peaks are matched well [5]. As the Al layer has been etched out from Ti_3AlC_2, the first peak (002) in $Ti_3C_2T_z$ XRD profile (Fig. 3.1b) shifts from higher to lower angle and the intensity is increased, which indicates the Al has been removed [34]. The shift in (002) peak also indicates the enlargement of the d-spacing, leading to larger gallery between the carbide blocks for lithium intercalation. The (002) peak and higher-order (00l) peaks (Fig. 3.1b) can be used to estimate the d-spacing of $Ti_3C_2T_z$, which was found to be 9.91 Å, consistent with previous XRD characterizations [35]. The extra peak at 24° belongs to TiO_2, indicating slightly oxidized sample which agrees with the Raman results [30].
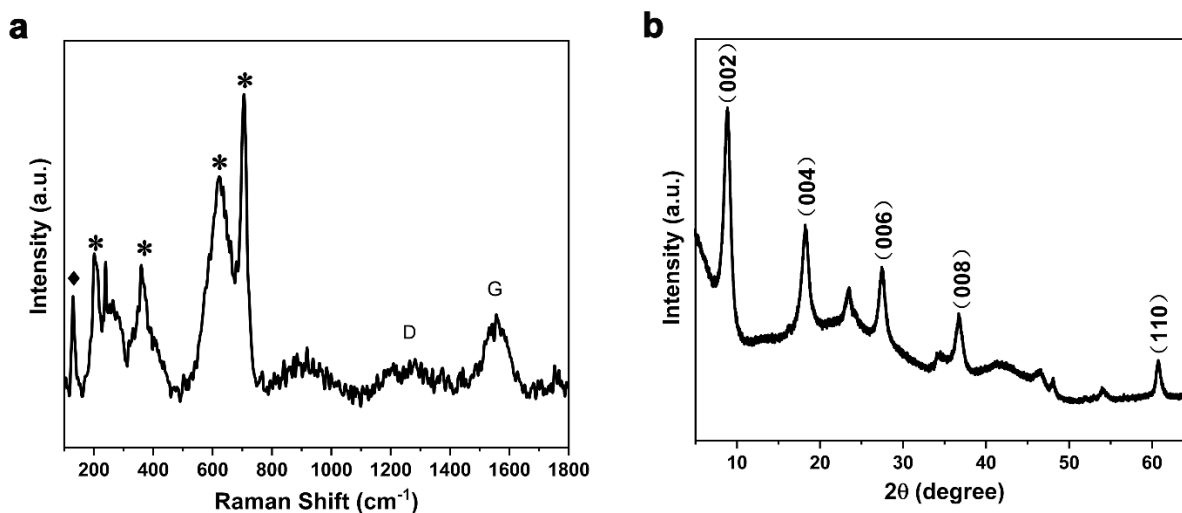

Fig 3.1. Characterization of $Ti_3C_2T_z$. (a) Raman spectrum and (b) XRD pattern of synthesized pristine $Ti_3C_2T_z$ powder

From the SEM results (Fig. 3.2a-b), the particle morphology of MXene $Ti_3C_2T_z$ material exhibits accordion-like structure resulting from HF etching of Ti_3AlC_2 layered structure, supporting Li-ion intercalation during the charging-discharging process and Li^+ ion shuttling. In the low magnification image (Fig. 3.2a), $Ti_3C_2T_z$ particle size is not uniformly distributed and varies from 4 µm to 25 µm in diameter.

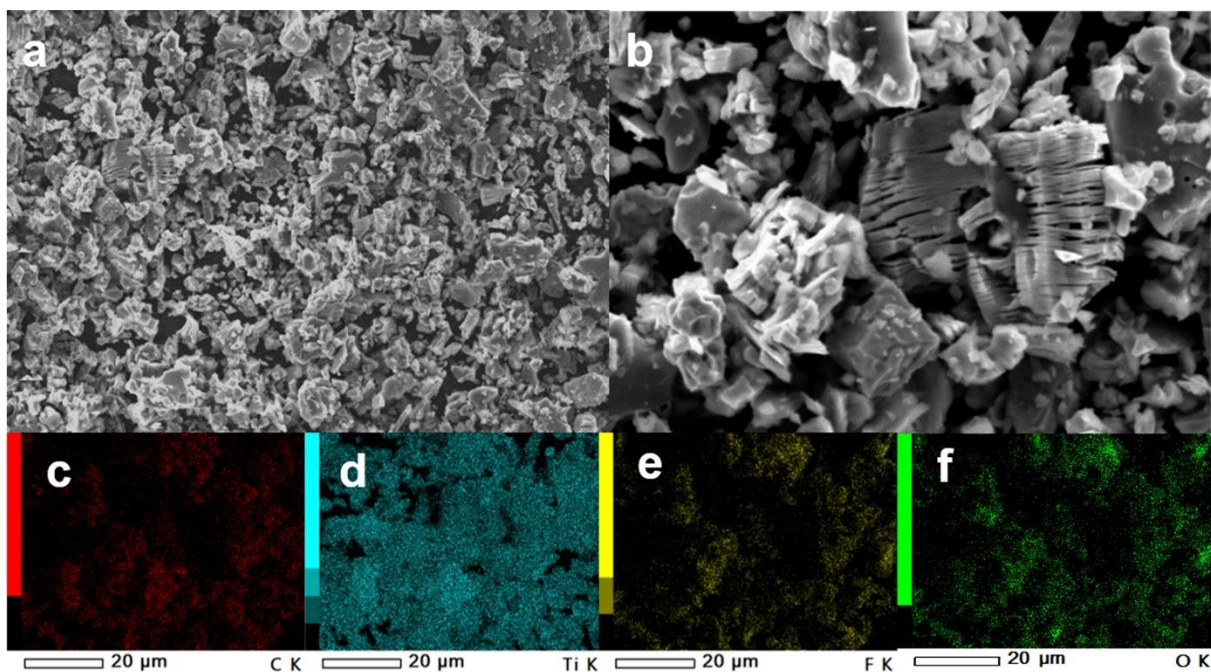**Fig 3.2.** SEM images of $Ti_3C_2T_z$ powder. (a) Low magnification and (b) High magnification $Ti_3C_2T_z$ SEM image, EDX of $Ti_3C_2T_z$ (c) Carbon, (d) Titanium, (e) Fluorine, and (f) Oxygen in low magnification image

Fig. 3.2c-f shows elemental mapping results. For Fig. 3.2a, where C and Ti are found to be evenly distributed, revealing their homogeneous distribution in synthesized material. Also, the surface-terminating functional groups, O and F are uniformly scattered around the $Ti_3C_2T_z$ nanoparticles. It's difficult to differentiate whether the O element belongs to O terminations or OH terminations, but both of them would have similar effects on electrochemical performance and thermal behavior [16]. Based on the elemental mapping results, the ratio of F and O terminations to Ti is 3.32:3 (F/Ti) and 3.12:3 (O/Ti), further confirming the F and O terminations existence in the $Ti_3C_2T_z$ particles, which affect the thermal and electrochemical performance. The Al/Ti ratio is 0.17:3, where some of this can be attributed to the aluminum SEM sample holder. Residual Al in the multilayer structure would reduce the specific capacity during charge and discharge cycles [9].

3.4.2 Electrochemical Performance

In order to analyze the thermal runaway behavior, $Ti_3C_2T_z$ and graphite electrodes were discharged to different states of charge (SOCs). The fully lithiated state was defined as 100% SOC (5 mV vs Li/Li$^+$) and the fully delithiated state was defined as 0% SOC (3 V vs. Li/Li$^+$). The controlled study on thermal behavior between conventional graphite and $Ti_3C_2T_z$ was performed to analyze their thermal response at elevated temperature. Both $Ti_3C_2T_z$ and graphite LIB half-cells were cycled 5 times between 3 V and 5 mV (vs. Li/Li$^+$) for SEI formation and electrode activation.

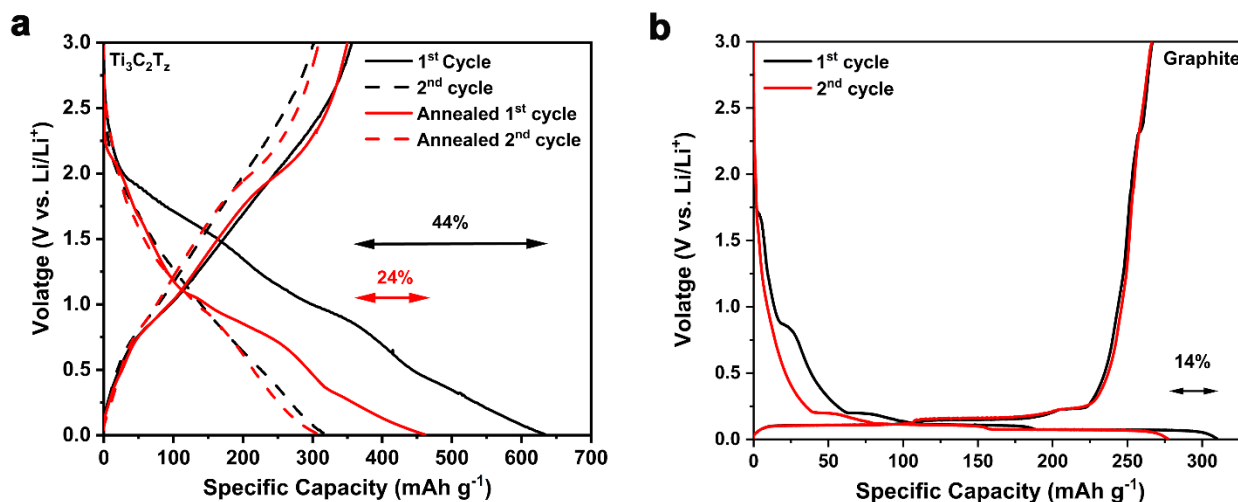**Fig 3.3.** Electrochemical performance of $Ti_3C_2T_z$ and graphite. Charge and discharge voltage profiles for (a) $Ti_3C_2T_z$ electrodes and (b) graphite electrode for Li-ion battery at 20 mA g^{-1}

Fig. 3.3 presents the voltage profiles of the initial 2 cycles from $Ti_3C_2T_z$ and graphite half-cells. For pristine $Ti_3C_2T_z$ electrode, the first cycle discharge and charge capacity are 633 mAh g^{-1} and 355 mAh g^{-1} with 44% irreversible capacity loss, ascribed to the reaction between Li and surface-terminating functional groups (O, OH, F) and SEI formation on the particles surface of $Ti_3C_2T_z$. The annealed $Ti_3C_2T_z$ anode has reduced irreversible capacity loss from 44% to 24%. In contrast, the graphite anode showed reduced irreversible capacity loss of 14%, where the side reactions with Li and SEI formation are reduced. The voltage profile of $Ti_3C_2T_z$ exhibited a discharge voltage plateau in the initial cycle at around 1.2 V, while pleateau disappears and voltage profile becomes more linear in the following cycles.

30

3.4.3 Thermal Analysis
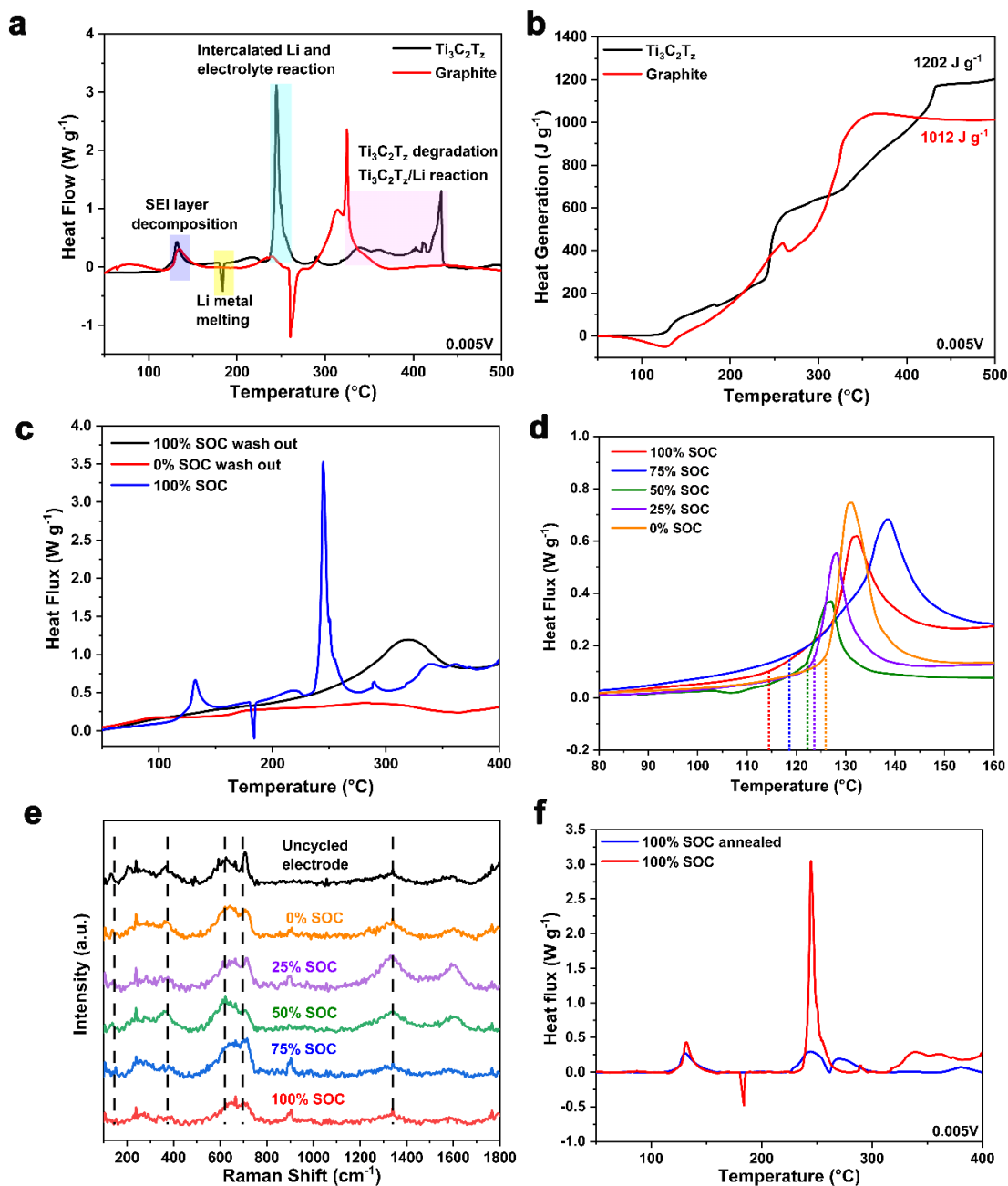
Fig 3.4. Thermal runaway profile of $Ti_3C_2T_z$ and graphite with Raman spectra. (a) DSC profiles and (b) total heat generation of $Ti_3C_2T_z$ and graphite electrode stabilized at 0.005V after 5 charged and discharge cycles at 20 mA g^{-1}, (c) DSC profiles of 100% and 0% SOC washout $Ti_3C_2T_z$ anode compare to DSC profile of pristine 100% SOC $Ti_3C_2T_z$, (d) DSC profiles of SEI decomposition at different SOCs, (e) Raman spectra of non-cycled electrodes and electrodes at different SOC, (f) DSC profiles of annealed $Ti_3C_2T_z$ and pristine $Ti_3C_2T_z$ electrode stabilized at 0.005V after 5 charged and discharge cycles at 20 mA g^{-1}.

Currently, there is no thermal stability investigation on the $Ti_3C_2T_z$ anode in the LIB system. However, graphite, as a typical anode material for LIBs, has been described in terms of its thermal runaway mechanism. With the knowledge of graphite, we categorized the thermal runaway of $Ti_3C_2T_z$ into three major stages: I) SEI degradation, II) intercalated Li and electrolyte reaction, and III) polyvinylidene difluoride (PVDF) binder reactions.

Stage I: SEI breakdown

The *ex-situ* DSC thermal analysis at the fully lithiated condition of $Ti_3C_2T_z$ and graphite are shown in Fig. 3.4a. At 100% SOC, the first exothermic peaks for $Ti_3C_2T_z$ and graphite anodes appeared at ~120 °C, corresponding to the SEI layer decomposition [36]. The SEI decomposition of graphite and $Ti_3C_2T_z$ exhibited similar onset temperature and exothermic peak intensity, indicating similar SEI composition formation on $Ti_3C_2T_z$ and the graphite anode. The SEI layer on graphite contains thermally metastable organic components ($ROCO_2Li$, $(CH_2OCO_2Li)_2$, and ROLi) and stable inorganic components ($LiCO_3$ and LiF) [24]. Cycling with the same electrolyte as the graphite anode, an analogous thermal decomposition mechanism of $Ti_3C_2T_z$ SEI can be proposed as:

$$(CH_2OCO_2Li)_2 \rightarrow Li_2CO_3 + C_2H_4 + CO_2 + 0.5O_2 \tag{3.1}$$
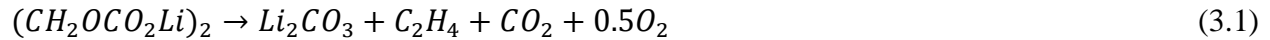
Another possible reaction is the intercalated Li reacting with $(CH_2OCO_2Li)_2$ [37]

$$2Li + (CH_2OCO_2Li)_2 \rightarrow 2Li_2CO_3 + C_2H_4 \tag{3.2}$$

The $LiPF_6$ in the electrolyte also participates in SEI decomposition as a strong Lewis acid attacking the C-O bond and further impels SEI decomposition [38]. The heat generated from SEI decomposition leads to a series of reactions including the reactions involving intercalated Li reacting at a higher temperature.

BET surface area measurement results were consistent with our observation in electrochemical performance. The specific surface area of $Ti_3C_2T_z$ is 3.3 m^2 g^{-1}, which is larger than graphite (2.2 m^2 g^{-1}). The nitrogen sorption isotherms and pore size distribution of $Ti_3C_2T_z$ and graphite are shown in Fig. 3.S1. The pore size of graphite is narrowly distributed from 3 nm to 5 nm. In contrast, $Ti_3C_2T_z$ has pore size distribution, varies between 3 to 10 nm, consistent. Both materials are mesoporous, but $Ti_3C_2T_z$ has a higher peak centered at 1.75 nm and 3 nm providing more surface area and mesopores for lithium-ion interaction, matching with the observation on electrochemical performance [30]. The SEI formation on the anode is known to be closely related

to the surface area. The surface accessed to N_2 in the BET experiment would be the same surface accessed to the electrolyte for SEI formation while cycling, and the BET results precisely reflected the SEI generation region [39]. As the surface area increases, a higher amount of SEI layer will form, which increases the irreversible capacity and overall heat generation when it decomposes [2]. Obtained results from $Ti_3C_2T_z$ and graphite anode are reasonably consistent with the analysis, as the higher surface area of $Ti_3C_2T_z$ corresponds to higher exothermic peak.

SEI decomposition at different SOCs

Since SEI decomposition is the first stage that happens in the thermal runaway process and initiates succeeding thermal runaway reactions, it is important to understand the SEI decomposition at different lithiation states. In order to elucidate this effect, the DSC profiles of $Ti_3C_2T_z$ anodes at different SOCs (Fig. 3.4d) were collected. Table. 3.2 summarizes the temperature and heat generations of each SOC. The SOCs were defined in terms of the cell voltage states, 3V (0% SOC), 2.25V (75% SOC), 1.5V (50% SOC), 0.75V (25% SOC), 0.005V (100% SOC).

Table 3.1. SEI decomposition at different SOCs. Onset temperature and heat generation from SEI degradation at different SOCs of $Ti_3C_2T_z$.

SOC (%)	Onset temperature (°C)	Heat generation $(J\ g^{-1})$
0	125	51.19
25	123	32.18
50	122	23.92
75	118	85.08
100	114	59.45

In Fig. 3.4d, as SOC increases, the onset temperature of SEI decomposition decreases (Table. 1), which means the SEI layer is more unstable as more lithium-ion is intercalated into the layered structure. However, the heat generation from SEI decomposition is not linearly related to SOCs. Previous graphite anode lithiation dependent studies on SEI thermal decomposition in both Li and K systems do not exhibit the same tendency, where both the onset temperature and heat generation increases with the degree of lithiation [23]. The conflict in heat generation is ascribed to two

reasons. First, the surface-terminating funcional groups are able to bind extra Li^+ and affect the thermal behavior. This makes the amount of Li participating in SEI decomposition (Reaction. 2) is hard to quantify. Second, the voltage plateau of $Ti_3C_2T_z$ might affect the heat generation. Near the voltage plateau (~1.2V), at 50% SOC and 25% SOC, the heat generation is slightly less than other SOCs.

In order to further investigate the structural evolution of $Ti_3C_2T_z$ anode during the lithiation process and its impact on the thermal runaway, Raman spectroscopy was utilized to analyze the process. Fig. 3.4e shows the Raman spectra for the uncycled electrode and cycled electrodes at different SOCs. Most of the stretching bands remain the same in the cycled and uncycled electrodes, but the 610 cm^{-1} band has shifted to higher energy in the cycled electrodes. Furthermore, from 0% SOC to 100% SOC, this band has shifted to higher energy indicating more lithium ions intercalated, so the layer thickness decreased as the bonds harden [28]. A new band at ~705 cm^{-1} emerged in cycled $Ti_3C_2T_z$ electrodes, which belongs to O terminations on the surface of the electrode [40]. This Raman band appearance of cycled electrodes possibly belongs to SEI formation on the surface with organic polymers and compounds.

Stage II: Intercalated Li and electrolyte reaction

The intercalated lithium protected by the SEI layer is exposed to electrolyte after SEI decomposition. In Fig. 3.4a, intercalated Li reacted with electrolyte at higher temperatures in $Ti_3C_2T_z$ (236 °C) compared to graphite (219 °C). This exothermic reaction in graphite anodes is centered at 238 °C, which is consistent with the previous research [39]. The reaction happens between intercalated Li and organic EC solvent and produces C_2H_4 and Li_2CO_3 [41]. The chemical reaction is proposed as following [41]:

$$2Li + C_3H_4O_3 \rightarrow Li_2CO_3 + C_2H_4 \tag{3.3}$$

In order to demonstrate the reactions happening between intercalated Li and electrolyte solvent in $Ti_3C_2T_z$ anode, the fully lithiated anodes were washed in DMC and dried overnight to remove electrolyte. The DSC result of the washed anode (Fig. 3.4c) shows no exothermic peak for the SEI decomposition and intercalated Li/electrolyte reactions, proving the peak at ~236 °C belongs to intercalated Li/electrolyte reaction and that the SEI was washed out by DMC. Additionally, the endothermic peak on $Ti_3C_2T_z$ around 180 °C corresponds to the thin lithium layer melting on the fully lithiated $Ti_3C_2T_z$ electrode surface. This thin lithium layer is captured by $Ti_3C_2T_z$ surface-

terminating functional groups that strongly influence the first cycle irreversible capacity loss. This extra plated lithium also participates in the intercalated Li/electrolyte reaction. Although the surface lithium layer renders a higher capacity for $Ti_3C_2T_z$ anode, it contributes to extra exothermic heat generation. Another possible reaction is that the PF_5 from $LiPF_6$ can attack electron-ion pairs in carbonyl groups (e.g. in EC) and generate transesterification products (PEO polymers and CO_2) [41,42].

In order to improve the thermal stability of $Ti_3C_2T_z$, the pristine $Ti_3C_2T_z$ was calcined in an Ar atmosphere at 400 °C for 20 minutes in order to remove structural water and modify the surface terminations. After this annealing process, OH terminations are either removed or converted into O termination [28]. This annealing process can provide higher thermal stability and better electrochemical performance [28]. In Fig. 3.3a, annealed $Ti_3C_2T_z$ electrode materials in half-cells show first cycle irreversible capacity loss, which has decreased to 24% from 44% with the same second cycle charge/discharge capacity compared to pristine, indicating a significant reduction of lithium loss during the first cycle. In Fig. 3.4f, the lithium melting peak around 180 °C disappears in the annealed sample, and the intercalated Li/electrolyte reaction peak intensity is decreased. With the surface modification, the $Ti_3C_2T_z$ electrode doesn't trap extra lithium in the structure. Therefore, the heat generation in stage II has decreased from 245 J g^{-1} to 75 J g^{-1}.

Different from 100% SOC, the intercalated Li/electrolyte reaction isn't observed in 0% SOC (Fig. 3.S2), because the intercalated lithium is limited. Instead of the sharp exothermic peak, the endothermic peak in both materials between 200 °C and 300 °C indicates the $LiPF_6$ melting, which agrees with the melting point of $LiPF_6$ (200 °C).

Stage III: Intercalated Li, $Ti_3C_2T_z$, and PVDF binder reaction

In graphite anodes (Fig. 3.4a), the exothermic peak from 282 °C to 366 °C is attributed to intercalated Li/PVDF reaction, as described in the literature [43,44]. Dehydrochlorination of PVDF due to the highly reductive lithium generates LiF and H_2. The possible reaction (Reaction. 4) is proposed by Du Pasquier *et al.* [43] and verified by Wang *et al.* [45]

$$-[CH_2 - CF_2] - +Li^+ + e^- \rightarrow LiF + -[CH = CF] - +0.5H_2 \qquad (4)$$
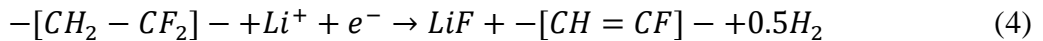
However, the exothermic peak of $Ti_3C_2T_z$ appears at a much higher temperature (318 °C) than graphite (Fig. 3.4a). This broad exothermic peak arises because of three reasons: 1. intercalated Li/PVDF reaction, 2. intercalated Li/$Ti_3C_2T_z$ reaction, and 3. $Ti_3C_2T_z$ degradation. In Fig. 3.4c, the

washed 100% SOC $Ti_3C_2T_z$ anode still shows an exothermic peak starting around 280 °C, comparing to the washed 0% SOC anode. It proves the reaction between intercalated Li and $Ti_3C_2T_z$, consistent with the results in Fig. 3.S3a. Additionally, the evaporation of surface-terminating functional groups also generate heat after 380 °C (Fig. 3.S3b), matching with previous literature on OH and F evaporation [33,34]. Both functional group evaporation and their reaction with intercalated Li distributes heat to the thermal runaway process in 100% SOC after 300 °C (Fig. 3.4a).

The surface termination modification (Fig. 3.4f) brings the entire exothermic peak of stage III from 318 °C to 216 °C and reduces heat generation. This exothermic peak corresponds to the intercalated Li/PVDF reaction, as it has same onset temperature as graphite, but it generates less heat than graphite. The exothermic reactions from 1. intercalated Li and $Ti_3C_2T_z$ and 2. $Ti_3C_2T_z$ degradation have been completely removed, indicating those reactions mostly happen between intercalated Li and structural water or OH terminations.

In the entire thermal runaway process, the total heat generation (Fig. 3.4b) from pristine $Ti_3C_2T_z$ (1202 J/g) is slightly higher than graphite (1012 J g^{-1}) due to the exothermic reactions form surface plated lithium and terminal groups. However, capacity specific heat generation of $Ti_3C_2T_z$ (2.68 J g^{-1}) is lower than graphite (2.72 J g^{-1}), showing that there is less density of heat generation in the thermal runaway process for $Ti_3C_2T_z$.

3.4.4 In-situ Thermal Analysis

The *ex-situ* thermal runaway analysis by DSC has identified the thermal behavior of individual components (electrode, electrolyte, and SEI) in $Ti_3C_2T_z$ anodes, where the overview of its thermal safety aspects can be preliminarily concluded. However, DSC analysis has its limitations. First, the limited sample size (< 5 mg) of DSC restricts the investigation of the chemical stability of the entire coin cell. Second, the obtained results are highly dependent on the sample preparation process, where many artifacts might be introduced to the sample (e.g. the ratio of electrode material and electrolyte, environmental atmosphere). Thus, *in-situ* thermal analysis turns out to be necessary for a comprehensive thermal runaway study. In this case, the *in-situ* thermal stability analysis of $Ti_3C_2T_z$ (Fig. 3.5a) was conducted in multiple module calorimetry (MMC) for CR-2032 coin cells. With large operation size (gram-size), MMC can be utilized to measure the heat generation and phase change of the entire coin cell from room temperature to 300 °C with 0.001°

temperature resolution and < 3% energy measurement accuracy, reflecting explicit thermal runaway behavior [46].
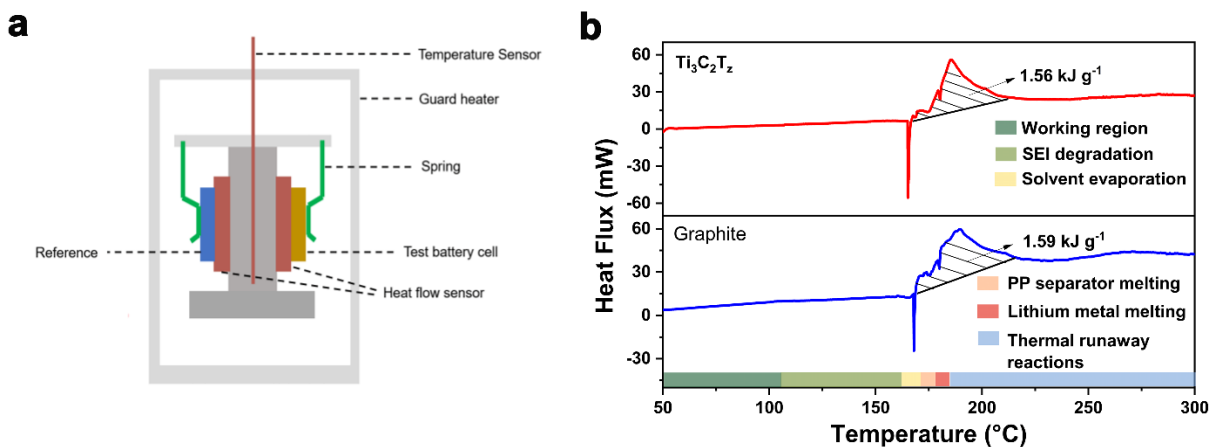

Fig 3.5. In-situ thermal study. (A) Schematic of multiple module calorimetry chamber, and (B) in-situ thermal analysis using multimode calorimetry on $Ti_3C_2T_z$ and graphite half-cell

The $Ti_3C_2T_z$ and graphite half cells were assembled and discharged to 100% SOC before being loaded to MMC. In Fig. 3.5b, $Ti_3C_2T_z$-lithium half-cell and graphite-lithium half-cell yielded analogous MMC profiles. Around 120 °C, there is no exothermic peak on either cell, which appeared in the DSC profile as SEI degradation in both materials. The mass and thickness (typically 1-8 nm) of SEI are extremely small compared to the entire coin cell, and this small amount of heat has been absorbed immediately by the liquid in the coin cell. For the entire process, there are three major endothermic processes. First, at 165 °C, the EC/DEC solvent for $LiPF_6$ electrolyte has a phase transition, which corresponds to liquid solvent evaporation. In consequence, this evaporation increases the pressure inside the coin cell. Second, the PP gasket and separator melts around 175 °C, which further damages the integrity of the coin cell. With the pressure increasing and gasket melting, the coin cell deforms after 175 °C, causing leakage and baseline shifting in the MMC profile (Fig. 3.5b). Third, at 180 °C, a small endothermic peak appears on both coin cells, which corresponds to lithium foil melting. Because of the solvent evaporation, complex thermal runaway reactions occur and generate a large amount of heat after 167 °C for both cells. The graphite half-cell (1.59 kJ g⁻¹) had slightly higher heat generation from 167 °C to 212 °C than $Ti_3C_2T_z$ half-cell (1.56 kJ g⁻¹). In these exothermic processes (after 167 °C), the heat generation belongs to the intercalated Li and electrolyte reaction, which matches with DSC data at the same temperature range [43]. Overall, even though both coin cells experienced pressure

37

build-up and disintegration, the $Ti_3C_2T_z$ half-cell still generated less heat than graphite during the entire process.

3.5 Conclusion

In this work, the thermal stability and safety characteristics of $Ti_3C_2T_z$ anode was studied by *ex-situ* and *in-situ* thermal analysis techniques. At 100% SOC, the thermal runaway for $Ti_3C_2T_z$ is initiated by SEI decomposition at ~120 °C, similar to graphite. However, capacity specific heat generation of $Ti_3C_2T_z$ anode (2.68 J mAh^{-1}) is demonstrated to be lower than graphite (2.72 J mAh^{-1}). During SEI decomposition, both materials showed an exothermic peak at almost the same temperature.

The heat generated from $Ti_3C_2T_z$ SEI is highly dependent on the SOC. Its decomposition onset temperature decreases as more Li^+ intercalated into the layered structure, indicating reduced thermal stability. At 100% SOC, the intercalated Li/electrolyte reaction appears at higher temperatures in $Ti_3C_2T_z$ (236 °C) compared to graphite (219 °C) generating more heat. A chemically deposited thin lithium layer on the $Ti_3C_2T_z$ anode surface is confirmed by DSC. This Li layer melts at 180 °C and contributes to extra heat generation due to its reaction with electrolyte. The surface-terminating functional groups on $Ti_3C_2T_z$ have a significant impact on electrochemical performance, corresponding to higher irreversible capacity in the first cycle. The liberation of these terminations above 380 °C affects the overall thermal behavior of $Ti_3C_2T_z$ anode. With the annealing process at 400 °C, the $Ti_3C_2T_z$ electrode's thermal stability is improved and becomes slightly safer than graphite. The heat generated from the intercalated Li/electrolyte reaction has significantly reduced from 245 J g^{-1} to 75 J g^{-1}. The exothermic reactions between intercalated Li and terminations were eliminated, and the reaction with PVDF generates less heat than graphite.

The *in-situ* thermal analysis conducted by MMC confirms that there is less heat generation from $Ti_3C_2T_z$ half-cell (1.56 kJ g^{-1}) than graphite half-cell (1.59 kJ g^{-1}) in the entire coin cell and that the coin cell deformation is due to solvent evaporation and polypropylene gasket meltdown. In summary, $Ti_3C_2T_z$ anode exhibits similar thermal behavior at each stage compared to graphite anode but generates less heat. Tailoring the surface-terminating functional groups on $Ti_3C_2T_z$ surface allows improvement in the electrochemical performance and thermal stability.

Acknowledgments

3.7 References

[1]   J.B. Goodenough, Y. Kim, Challenges for Rechargeable Li Batteries [†], Chem. Mater. 22 (2010) 587–603. https://doi.org/10.1021/cm901452z.

[2]   X. Feng, M. Ouyang, X. Liu, L. Lu, Y. Xia, X. He, Thermal runaway mechanism of lithium ion battery for electric vehicles: A review, Energy Storage Mater. 10 (2018) 246–267. https://doi.org/10.1016/j.ensm.2017.05.013.

[3]   F. Perton, C. Audry, P. Biensan, A. De Guibert, G. Blanc, M. Broussely, A new method to study Li-ion cell safety: laser beam initiated reactions on both charged negative and positive electrodes, J. Power Sources. 98 (2001).

[4]   E. Allcorn, S.O. Kim, A. Manthiram, Thermal stability of active/inactive nanocomposite anodes based on Cu_2Sb in lithium-ion batteries, J. Power Sources. 299 (2015) 501–508. https://doi.org/10.1016/j.jpowsour.2015.09.020.

[5]   M. Naguib, V.N. Mochalin, M.W. Barsoum, Y. Gogotsi, 25th anniversary article: MXenes: A new family of two-dimensional materials, Adv. Mater. 26 (2014) 992–1005. https://doi.org/10.1002/adma.201304138.

[6]   M. Naguib, J. Halim, J. Lu, K.M. Cook, L. Hultman, Y. Gogotsi, M.W. Barsoum, New two-dimensional niobium and vanadium carbides as promising materials for li-ion batteries, J. Am. Chem. Soc. 135 (2013) 15966–15969. https://doi.org/10.1021/ja405735d.

[7]   J. Come, M. Naguib, P. Rozier, M.W. Barsoum, Y. Gogotsi, P.-L. Taberna, M. Morcrette, P. Simon, A Non-Aqueous Asymmetric Cell with a Ti 2 C-Based Two-Dimensional Negative Electrode , J. Electrochem. Soc. 159 (2012) A1368–A1373. https://doi.org/10.1149/2.003208jes.

[8]   M. Naguib, B. Dyatkin, V. Presser, M.W. Barsoum, P. Simon, Y. Gogotsi, J. Come, P.-L. Taberna, MXene: a promising transition metal carbide anode for lithium-ion batteries, Electrochem. Commun. 16 (2012) 61–64. https://doi.org/10.1016/j.elecom.2012.01.002.

[9]   D. Xiong, X. Li, Z. Bai, S. Lu, Recent Advances in Layered Ti3C2Tx MXene for Electrochemical Energy Storage, Small. 14 (2018) 1–29. https://doi.org/10.1002/smll.201703419.

[10]   J. Xu, N. Yang, S. Heuser, S. Yu, A. Schulte, H. Schönherr, X. Jiang, Achieving Ultrahigh Energy Densities of Supercapacitors with Porous Titanium Carbide/Boron-Doped Diamond Composite Electrodes, Adv. Energy Mater. 9 (2019) 1–11. https://doi.org/10.1002/aenm.201803623.

[11] M.R. Lukatskaya, O. Mashtalir, C.E. Ren, Y. Dall'Agnese, P. Rozier, P.L. Taberna, M. Naguib, P. Simon, M.W. Barsoum, Y. Gogotsi, Cation intercalation and high volumetric capacitance of two-dimensional titanium carbide, Science (80-.). 341 (2013) 1502–1505. https://doi.org/10.1126/science.1241488.

[12] M. Naguib, M.W. Barsoum, Y. Dall'Agnese, H.L. Zhuang, Y. Gogotsi, P.R.C. Kent, Y. Xie, Prediction and Characterization of MXene Nanosheet Anodes for Non-Lithium-Ion Batteries, ACS Nano. 8 (2014) 9606–9615. https://doi.org/10.1021/nn503921j.

[13] S. Kajiyama, L. Szabova, K. Sodeyama, H. Iinuma, R. Morita, K. Gotoh, Y. Tateyama, M. Okubo, A. Yamada, Sodium-Ion Intercalation Mechanism in MXene Nanosheets, ACS Nano. 10 (2016) 3334–3341. https://doi.org/10.1021/acsnano.5b06958.

[14] M. Naguib, R.A. Adams, Y. Zhao, D. Zemlyanov, A. Varma, J. Nanda, V.G. Pol, Electrochemical performance of MXenes as K-ion battery anodes, Chem. Commun. 53 (2017) 6883–6886. https://doi.org/10.1039/c7cc02026k.

[15] P. Lian, Y. Dong, Z.S. Wu, S. Zheng, S. Wang, C. Sun, J. Qin, X. Shi, X. Bao, Alkalized Ti3C2 MXene nanoribbons with expanded interlayer spacing for high-capacity sodium and potassium ion batteries, Nano Energy. 40 (2017) 1–8. https://doi.org/10.1016/j.nanoen.2017.08.002.

[16] D. Er, J. Li, M. Naguib, Y. Gogotsi, V.B. Shenoy, Ti3C2 MXene as a high capacity electrode material for metal (Li, Na, K, Ca) ion batteries, ACS Appl. Mater. Interfaces. 6 (2014) 11173–11179. https://doi.org/10.1021/am501144q.

[17] X. Wang, T.S. Mathis, K. Li, Z. Lin, L. Vlcek, T. Torita, N.C. Osti, C. Hatter, P. Urbankowski, A. Sarycheva, M. Tyagi, E. Mamontov, P. Simon, Y. Gogotsi, Influences from solvents on charge storage in titanium carbide MXenes, Nat. Energy. 4 (2019) 241–248. https://doi.org/10.1038/s41560-019-0339-9.

[18] F. Kong, X. He, Q. Liu, X. Qi, Y. Zheng, R. Wang, Y. Bai, Effect of Ti3AlC2 precursor on the electrochemical properties of the resulting MXene Ti3C2 for Li-ion batteries, Ceram. Int. 44 (2018) 11591–11596. https://doi.org/10.1016/j.ceramint.2018.03.223.

[19] M. Naguib, M. Kurtoglu, V. Presser, J. Lu, J. Niu, M. Heon, L. Hultman, Y. Gogotsi, M.W. Barsoum, Two-dimensional nanocrystals produced by exfoliation of Ti 3AlC 2, Adv. Mater. 23 (2011) 4248–4253. https://doi.org/10.1002/adma.201102306.

[20] R.A. Adams, A. Varma, V.G. Pol, Carbon Anodes for Nonaqueous Alkali Metal-Ion Batteries and Their Thermal Safety Aspects, Adv. Energy Mater. 1900550 (2019) 1900550. https://doi.org/10.1002/aenm.201900550.

[21] O. Mashtalir, M. Naguib, V.N. Mochalin, Y. Dall'Agnese, M. Heon, M.W. Barsoum, Y. Gogotsi, Intercalation and delamination of layered carbides and carbonitrides, Nat. Commun. 4 (2013) 1–7. https://doi.org/10.1038/ncomms2664.

[22] J. Halim, S. Kota, M.R. Lukatskaya, M. Naguib, M.Q. Zhao, E.J. Moon, J. Pitock, J. Nanda, S.J. May, Y. Gogotsi, M.W. Barsoum, Synthesis and Characterization of 2D Molybdenum Carbide (MXene), Adv. Funct. Mater. 26 (2016) 3118–3127. https://doi.org/10.1002/adfm.201505328.

[23]   J. Zhou, S. Gao, Z. Guo, Z. Sun, Ti-enhanced exfoliation of V2AlC into V2C MXene for lithium-ion battery anodes, Ceram. Int. 43 (2017) 11450–11454. https://doi.org/10.1016/j.ceramint.2017.06.016.

[24]   K. Liu, Y. Liu, D. Lin, A. Pei, Y. Cui, Materials for lithium-ion battery safety, Sci. Adv. 4 (2018). https://doi.org/10.1126/sciadv.aas9820.

[25]   P. Verma, P. Maire, P. Novák, A review of the features and analyses of the solid electrolyte interphase in Li-ion batteries, Electrochim. Acta. 55 (2010) 6332–6341. https://doi.org/10.1016/j.electacta.2010.05.072.

[26]   E.P. Roth, D.H. Doughty, J. Franklin, DSC investigation of exothermic reactions occurring at elevated temperatures in lithium-ion anodes containing PVDF-based binders, J. Power Sources. 134 (2004) 222–234. https://doi.org/10.1016/j.jpowsour.2004.03.074.

[27]   A. Kvasha, C. Gutiérrez, U. Osa, I. de Meatza, J.A. Blazquez, H. Macicior, I. Urdampilleta, A comparative study of thermal runaway of commercial lithium ion cells, Energy. 159 (2018) 547–557. https://doi.org/10.1016/j.energy.2018.06.173.

[28]   R.B. Rakhi, B. Ahmed, M.N. Hedhili, D.H. Anjum, H.N. Alshareef, Effect of Postetch Annealing Gas Composition on the Structural and Electrochemical Properties of Ti$_2$CT$_x$ MXene Electrodes for Supercapacitor Applications, Chem. Mater. 27 (2015) 5314–5323. https://doi.org/10.1021/acs.chemmater.5b01623.

[29]   Y. Dong, Z.S. Wu, S. Zheng, X. Wang, J. Qin, S. Wang, X. Shi, X. Bao, Ti3C2 MXene-Derived Sodium/Potassium Titanate Nanoribbons for High-Performance Sodium/Potassium Ion Batteries with Enhanced Capacities, ACS Nano. 11 (2017) 4792–4800. https://doi.org/10.1021/acsnano.7b01165.

[30]   J.F. Zhu, Y. Tang, C.H. Yang, F. Wang, M.J. Cao, Composites of TiO2 nanoparticles deposited on Ti3C2 mxene nanosheets with enhanced electrochemical performance, J. Electrochem. Soc. 163 (2016) A785–A791. https://doi.org/10.1149/2.0981605jes.

[31]   X. Tang, X. Guo, W. Wu, G. Wang, 2D Metal Carbides and Nitrides (MXenes) as High-Performance Electrode Materials for Lithium-Based Batteries, Adv. Energy Mater. 8 (2018) 1–21. https://doi.org/10.1002/aenm.201801897.

[32]   H. Yu, Y. Wang, Y. Jing, J. Ma, C.F. Du, Q. Yan, Surface Modified MXene-Based Nanocomposites for Electrochemical Energy Conversion and Storage, Small. 1901503 (2019) 1–20. https://doi.org/10.1002/smll.201901503.

[33]   Z. Li, L. Wang, D. Sun, Y. Zhang, B. Liu, Q. Hu, A. Zhou, Synthesis and thermal stability of two-dimensional carbide MXene Ti3C2, Mater. Sci. Eng. B Solid-State Mater. Adv. Technol. 191 (2015) 33–40. https://doi.org/10.1016/j.mseb.2014.10.009.

[34]   O. Mashtalir, M. Naguib, B. Dyatkin, Y. Gogotsi, M.W. Barsoum, Kinetics of aluminum extraction from Ti3AlC2 in hydrofluoric acid, Mater. Chem. Phys. 139 (2013) 147–152. https://doi.org/10.1016/j.matchemphys.2013.01.008.

[35]   M. Ghidiu, M.R. Lukatskaya, M.Q. Zhao, Y. Gogotsi, M.W. Barsoum, Conductive two-dimensional titanium carbide "clay" with high volumetric capacitance, Nature. 516 (2015) 78–81. https://doi.org/10.1038/nature13970.

[36] R.A. Adams, A. Varma, V.G. Pol, Mechanistic elucidation of thermal runaway in potassium-ion batteries, J. Power Sources. 375 (2018) 131–137. https://doi.org/10.1016/j.jpowsour.2017.11.065.

[37] M.N. Richard, J.R. Dahn, Accelerating rate calorimetry study on the thermal stability of lithium intercalated graphite in electrolyte. I. Experimental, J. Electrochem. Soc. 146 (1999) 2068–2077. https://doi.org/10.1149/1.1391893.

[38] T. Gao, W. Lu, Mechanism and effect of thermal degradation on electrolyte ionic diffusivity in Li-ion batteries: A molecular dynamics study, Electrochim. Acta. 323 (2019) 134791. https://doi.org/10.1016/j.electacta.2019.134791.

[39] D.D. MacNeil, D. Larcher, J.R. Dahn, Comparison of the reactivity of various carbon electrode materials with electrolyte at elevated temperature, J. Electrochem. Soc. 146 (1999) 3596–3602. https://doi.org/10.1149/1.1392520.

[40] R. Cheng, T. Hu, H. Zhang, C. Wang, M. Hu, J. Yang, C. Cui, T. Guang, C. Li, C. Shi, P. Hou, X. Wang, Understanding the Lithium Storage Mechanism of Ti 3 C 2 T x MXene, J. Phys. Chem. C. 123 (2019) 1099–1109. https://doi.org/10.1021/acs.jpcc.8b10790.

[41] J. Jiang, J.R. Dahn, Effects of solvents and salts on the thermal stability of LiC6, Electrochim. Acta. 49 (2004) 4599–4604. https://doi.org/10.1016/j.electacta.2004.05.014.

[42] Q. Wang, J. Sun, X. Yao, C. Chen, Thermal stability of LiPF6/EC + DEC electrolyte with charged electrodes for lithium ion batteries, Thermochim. Acta. 437 (2005) 12–16. https://doi.org/10.1016/j.tca.2005.06.010.

[43] A. Du Pasquier, Differential Scanning Calorimetry Study of the Reactivity of Carbon Anodes in Plastic Li-Ion Batteries, J. Electrochem. Soc. 145 (1998) 472. https://doi.org/10.1149/1.1838287.

[44] J. ichi Yamaki, H. Takatsuji, T. Kawamura, M. Egashira, Thermal stability of graphite anode with electrolyte in lithium-ion cells, Solid State Ionics. 148 (2002) 241–245. https://doi.org/10.1016/S0167-2738(02)00060-7.

[45] Q. Wang, J. Sun, X. Yao, C. Chen, Thermal behavior of lithiated graphite with electrolyte in lithium-ion batteries, J. Electrochem. Soc. 153 (2006) 329–333. https://doi.org/10.1149/1.2139955.

[46] M.H. Parekh, A.D. Sediako, A. Naseri, M.J. Thomson, V.G. Pol, In Situ Mechanistic Elucidation of Superior Si-C-Graphite Li-Ion Battery Anode Formation with Thermal Safety Aspects, Adv. Energy Mater. 10 (2020) 1–12. https://doi.org/10.1002/aenm.201902799.
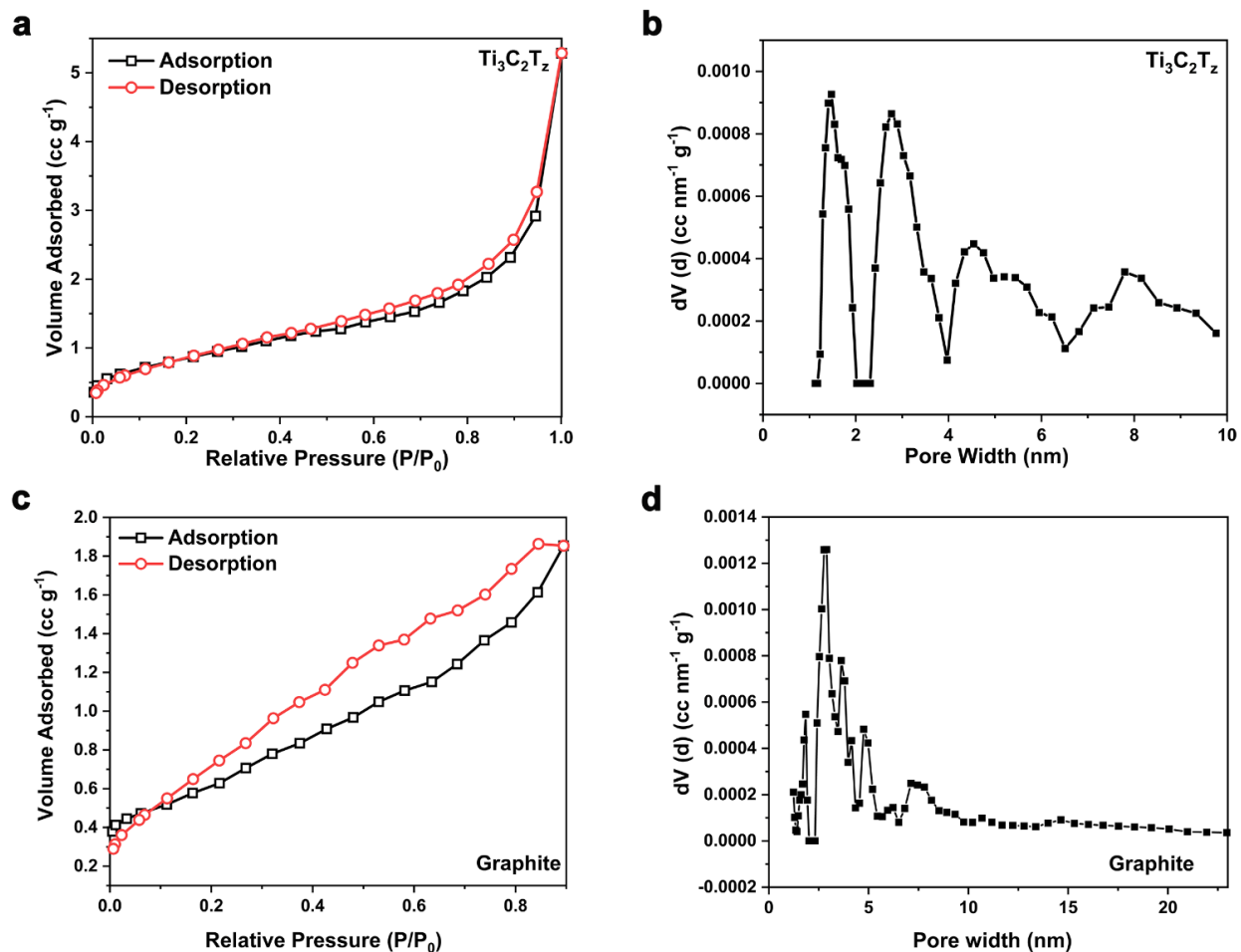
Supporting Information

Fig. 3.S1 Surface characterization of Ti3C2Tz and graphite. (a) Nitrogen sorption isotherms and (b) pore size distribution of Ti3C2Tz (c) Nitrogen sorption isotherms and (d) pore size distribution of graphite.

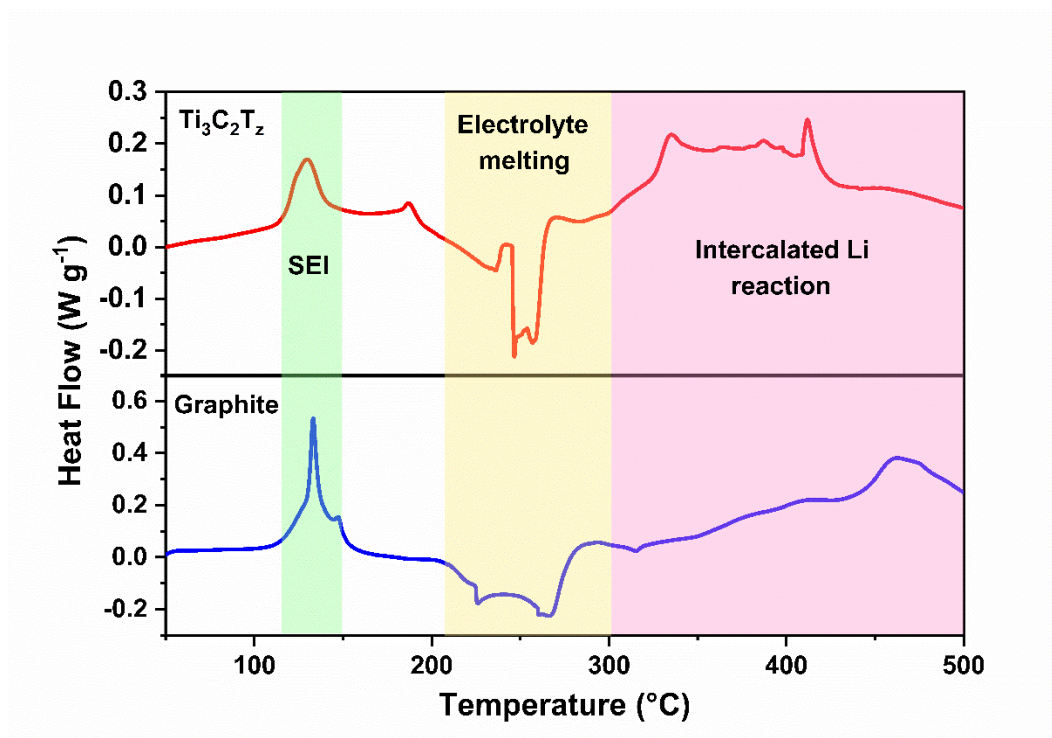**Fig. 3.S2** DSC profile of 0% SOC $Ti_3C_2T_z$ and graphite

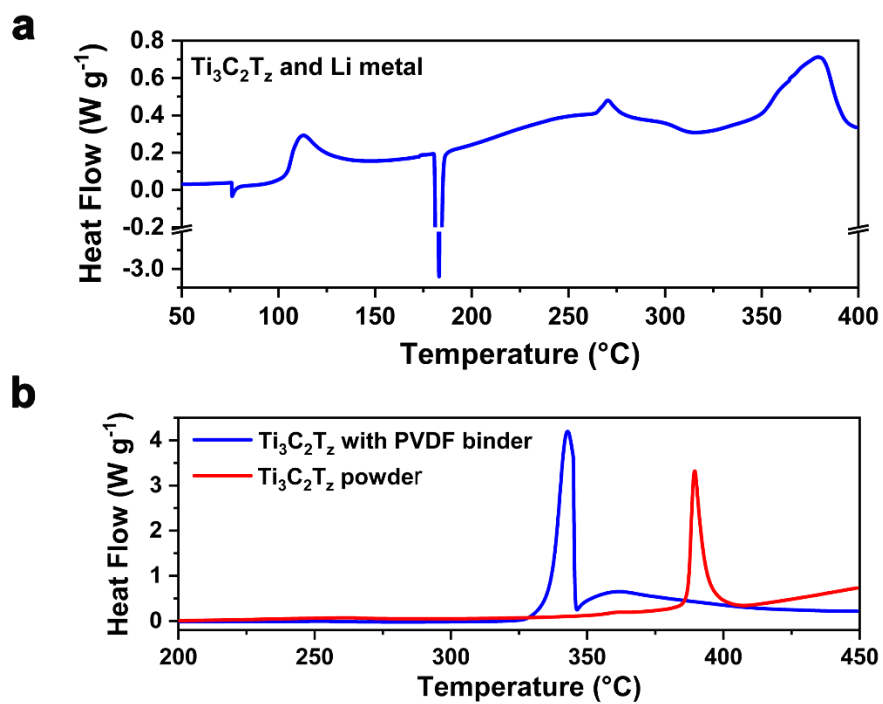**Fig. 3.S3** DSC Profile of Ti$_3$C$_2$T$_z$ with other components (a) Ti$_3$C$_2$T$_z$ and Lithium reaction (b) Ti$_3$C$_2$T$_z$ and Ti$_3$C$_2$T$_z$ with PVDF reaction
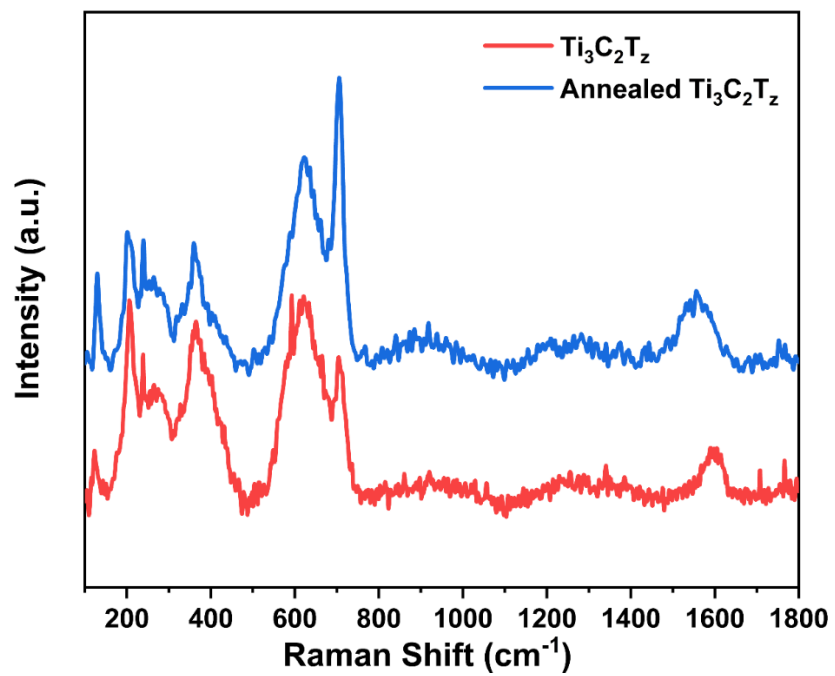
Fig. 3.S4 Raman spectra of annealed and pristine $Ti_3C_2T_z$

CHAPTER 4. SUMMARY AND RECOMMENDATION

4.1 Summary

In the thesis, I presented my work on elucidating the $Ti_3C_2T_z$ anode thermal behavior in LIBs. The thermal runaway for $Ti_3C_2T_z$ and graphite anodes of lithium ion batteries starts at a similar temperature (120 °C) with similar exothermic heat, corresponding to the solid electrolyte interface (SEI) degradation. By normalizing with capacity, $Ti_3C_2T_z$ (2.68J/mAh) generates less heat than graphite (2.72 J/mAh). The surface-terminating groups (-F, -OH, =O) on MXene surface have significantly affected the electrochemical performance including the coulombic efficiency and capacity. The SEI decomposition temperature and heat generation are highly dependent on the SOC. The thermal stability is reduced with more Li ion intercalated, and the onset temperature is decreased from 236 °C to 219 °C. After the annealing process, we could reduce the first cycle irreversible capacity loss from 44% to 24%. Also, the exothermic heat generated by reaction between intercalated Li and electrolyte is significantly reduced in annealed $Ti_3C_2T_z$.

4.2 Recommendations for Future Work

Beyond the $Ti_3C_2T_z$, this study provides a systematic way of investigating MXene material's thermal safety in LIBs. The strategy of research the exothermic reactions and the way to improve the safety could be applied on other kind of MXenes, such as Nb_2CT_z. The fundamental understanding of the thermal runaway mechanism of various MXene anode materials will provide scientific insights for the first time on their possible applications in the next generation commercial LIBs. Also, the surface-terminating groups' function and its behavior at high temperature has not been investigate thoroughly yet. Further investigation should be focus on the surface-terminating groups and its relationship with ion intercalation. In the exothermic reactions happened during the thermal runaway, more detailed and advanced instrument could be used to determine the products, such as time-of-flight mass spectroscopy. Accelerating rate calorimetry (ARC) is another calorimetry method which can test larger sample and determine self-heating rate by its adiabatic condition. The ARC used heat-wait-search mode, which increase the system temperature step by step until detecting the exothermic reaction. From ARC analysis, more information such as rate constants, activation energy could be obtained.